Summer 2016

# Copper Indium Disulfide Nanocrystal Luminescent Solar Concentrators

Ryan I. (Ryan Isaac) Sumner
*Western Washington University*, ryan.isaac.sumner@gmail.com

# Copper Indium Disulfide Nanocrystal Luminescent Solar Concentrators

By

Ryan Isaac Sumner

Accepted in Partial Completion
Of the Requirements for the Degree
Master of Science

Kathleen L. Kitto, Dean of the Graduate School

ADVISORY COMMITTEE

Chair, Dr. David L. Patrick

Dr. Steven Emory

Dr. Mark Peyron

# Masters Thesis

In presenting this thesis in partial fulfillment of the requirements for a master's degree at Western Washington University, I grant to Western Washington University the non-exclusive royalty –free right to archive, reproduce, distribute, and display the thesis in any and all forms, including electronic format, via any digital library mechanisms maintained by WWU.

I represent and warrant this as my original work, and does not infringe or violate any rights of others. I warrant that I have obtained written permissions from the owner of any third party copyrighted material included in these files.

I acknowledge that I retain ownership rights to the copyright of this work, including but not limited to the right to use all or part of this work in future works, such as articles or books.

Library users are granted permission for individual, research and non-commercial reproduction of this work for educational purposes only. Any further digital posting of this document requires specific permission from the author.

Any copying or publication of this thesis for commercial purposes, or for financial gain, is not allowed without my written permission.

Ryan Sumner

August 4, 2016

# Copper Indium Disulfide Nanocrystal Luminescent Solar Concentrators

A Thesis

Presented to

The Faculty of

Western Washington University

In Partial Fulfillment

Of the Requirements for the Degree

Master of Science

By

Ryan Isaac Sumner

August 2016

## Abstract

The sun is the most prominent renewable energy resource. Technologies such as photovoltaics (PVs) have yet to emerge as a cost effective alternative to non-renewable energy resources such as fossil fuels. Luminescent solar concentrators (LSC) possess the ability to lower the cost of solar energy by the reduction of the photovoltaic cell area and yet increase photovoltaic conversion efficiency. LSC's offer an attractive approach to concentrating both specular and diffuse light, which eliminates expensive solar tracking methods. Luminophores for LSC applications are often dominated by reabsorption losses and absorb a small part of the solar spectrum, which prevents LSC's from being a competitor in today's energy market. This thesis introduces a new class of luminophore for use in LSCs based on Copper Indium Disulfide (CIS). CIS has a broad absorption spectrum from the Ultraviolet to near-infrared with a tunable emission output, high photoluminescent quantum yield, and large effective stokes shift making them the current best LSC luminophore.

## Acknowledgements

Past and present members of the Patrick Solar Research Group:

Brian Carlson, Steven Eiselt, and Christian Erickson

Past and present members of the Gilbertson Solar Research Group:

Prof. John Gilbertson, David Brewster and Jared Chang

Collaborators at the University of Washington:

Prof. Daniel Gamelin, Dr. Liam Bradshaw, Troy Kilburn and Christian Erickson

Western Math Department:

Prof. Steve Mcdowell

Thesis Committee Members:

Prof. Steven Emory and Prof. Mark Peyron for their time, patience, and wisdom

My Family and Friends

Dr. David Patrick for his hours of mentoring, patience, and guidance

Dr. Arlan Norman for his charitable contribution to our research

The National Science Foundation and Environmental Protection Agency for their generous support.

# TABLE OF CONTENTS

ABSTRACT ..... IV

ACKNOWLEDGEMENTS ..... V

TABLE OF FIGURES ..... IX

CHAPTER 1: INTRODUCTION ..... 1

1.1 World energy consumption ..... 1

1.2 Potential Technologies for Renewable Energy ..... 3

1.2.1 Wind power ..... 3

1.2.2 Hydroelectric energy ..... 4

1.2.3 Biomass ..... 4

1.2.4 Geothermal energy ..... 5

1.2.5 Solar energy ..... 5

1.3 Solar Concentration ..... 6

1.3.1 Conventional designs ..... 6

1.3.2 Low-gain concentrators ..... 10

1.4 Summary ..... 11

CHAPTER 2: LUMINESCENT SOLAR CONCENTRATORS ..... 12

2.1 Introduction to Luminescent Solar Concentrators ..... 12

2.2 Design advantages ..... 13

2.3 LSC device performance ..... 14

2.4 Light propagation and loss ..... 15

2.4.1 Refraction ..... 16

2.4.2 Total Internal Reflection ..... 17

2.4.3 Escape cone ..... 17
2.4.4 Surface Scattering ..... 18
2.4.5 Light scattering from particles ..... 19
2.4.6 Matrix absorption ..... 20
2.5 Material Optimization for LSCs ..... 20
2.5.1 Waveguide Matrix ..... 20
2.5.2 Luminophores ..... 21
2.5.3 Organic Dyes ..... 22
2.5.4 Quantum Dots ..... 22
2.6 Summary ..... 23
CHAPTER 3: DOPED QUANTUM DOT LUMINESCENT SOLAR CONCENTRATORS ..... 24
3.1 $Mn^{2+}$ Doped Quantum Dots ..... 24
3.2 $Cu^{2+}$ CdSe Quantum Dots ..... 26
3.3 Copper indium disulfide quantum dots ..... 27
CHAPTER 4: EXPERIMENTAL METHODS ..... 29
4.1 CIS QD Synthesis ..... 29
4.2 Relative Quantum Yield ..... 32
4.3 Device Fabrication ..... 34
4.3.1 Creating the Polymer Solution ..... 34
4.3.2 LSC Shell ..... 35
4.3.3 Determining the Amount of QD's ..... 35
4.3.4 CIS LSC ..... 36
4.4 LSC Characterization ..... 37

4.4.1 Measuring the LSC ..... 37
4.4.2 Luminescent Spectrum Shift ..... 38
4.4.3 Calibrating the Fluorometer ..... 39
4.4.4 Experimental Limitations ..... 40
4.4.5 Correction Factor Using the McDowall Model ..... 41
4.5 Physical Characterization of the LSC Polymer ..... 44
4.5.1 FTIR Characterization ..... 44
4.5.2 TGA Characterization ..... 45
CHAPTER 5: RESULTS AND DISCUSSION ..... 47
5.1 Revisiting LSC Measurements ..... 47
5.2 Geometric Gain ..... 50
5.3 Nanocrystal Loading and Attenuation ..... 53
5.4 Conclusion ..... 57
REFERENCES ..... 59

## Table of Figures

Figure 1.1 Observed and projected world power consumption in TW.[1] ..... 1

Figure 1.2 Atmospheric carbon dioxide concentrations for the past 50 Years. Reproduced with permission from author.[3] ..... 2

Figure 1.3 Cross-sectional view of a Fresnel lens.[13] ..... 7

Figure 1.4 Diagram of a solar tower power plant.[15] ..... 8

Figure 1.5 Diagram of parabolic trough.[15] ..... 9

Figure 1.6 Diagram of solar dish plant.[16] ..... 10

Figure 1.7. Plasmonic light trapping geometries. Reproduced with permission from author.[19] ..... 11

Figure 2.1 A luminescent solar concentrator. ..... 12

Figure 2.2 Light propagation through an LSC. ..... 16

Figure 3.1 Photophysical diagram of $Mn^{2+}$ doped ZnSe quantum dots.[23] ..... 25

Figure 3.2 Photophysical diagram of $Cu^{+}$ doped CdSe quantum dots.[55] ..... 27

Figure 4.1 Experimental setup of shell growth for CIS QDs. ..... 31

Figure 4.2 Normalized emission and absorption of Lumogen red and CIS QDs. ..... 33

Figure 4.3 CIS QD LSCs presented in this work. ..... 37

Figure 4.4 Experimental setup for measuring CIS LSCs. ..... 38

Figure 4.5 Example calibration curve for CIS LSC TK106-1 ..... 40

Figure 4.6 FTIR spectra comparing the polymerized composite to laurylmethacryle monomer. ..... 45

Figure 4.7 Thermogravimetric analysis of composite to determine NC weight percent.46

Figure 5.2 Determination of nanocrystal absorbance to total extinction in LSC devices. ..... 49

Figure 5.3 LSC characterization and projected performance. ..... 50

Figure 5.4. Dependence of OPE and edge output irradiance on geometric gain. ..... 51

Figure 5.7 Dependence of waveguide attenuation on nanocrystal loading..... 53

Figure 5.8 LSC performance normalized to a QY of 1..... 55

Figure 5.9 Theoretical and actual performance of nanocrystal LSCs. ..... 56

# Chapter 1: Introduction

## 1.1 World energy consumption

The world's energy consumption is expected to nearly double in the next 25 years, from 20.2 terrawatt (TW), in 2010, to 39.0 TW in 2040.[1] The large increase in demand can be attributed to increasing global population and the growing economics of developing countries. Over 70 percent of the projected energy consumption for 2040 will come from non-renewable energy sources, which would primarily consist of coal, liquid, natural gas, and nuclear.[1] This projection

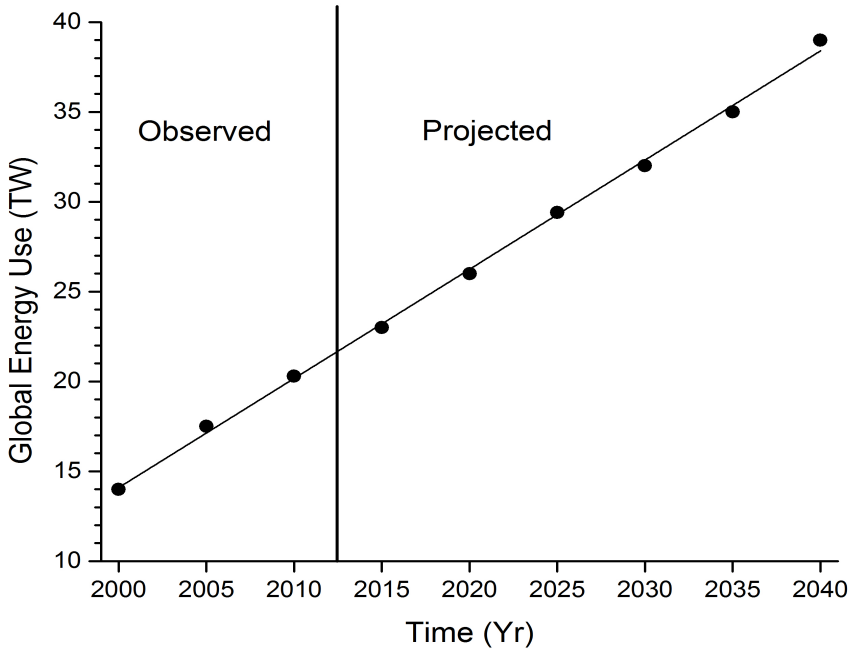


Figure 1.1 Observed and projected world power consumption in TW.[1]

leads to a problematic situation due to the correlation between non-renewable energy and greenhouse emissions. In 2010, non-renewable energy sources accounted for 80% of the total energy generation.[1] Non-renewable energy sources currently represent the most economically viable source of energy, however they've been shown to be correlated with an average rise in global temperature and climate change. [2]

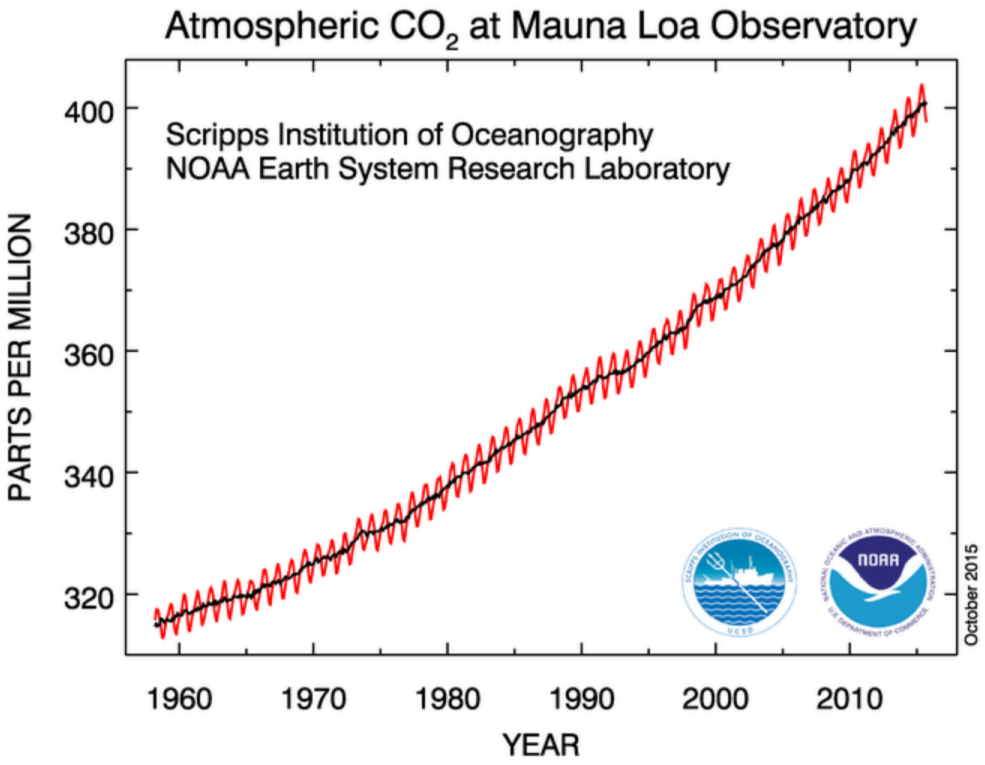


Figure 1.2 Atmospheric carbon dioxide concentrations for the past 50 Years. Reproduced with permission from author.[3]

The concentration of $CO_2$ in the atmosphere has risen steadily since its first recorded time by David Keeling in 1958.[3] The rise in atmospheric $CO_2$ can be seen in

Figure 1.2, and should be a basis of concern due to its impacts on global climate.[4] Despite environmental concerns, there are also geopolitical concerns associated with our national dependence on fossil fuels. The United States is a major producer of oil, coal, and natural gas. However, a large share of our petroleum consumption comes from foreign producers. The dependence on these foreign powers can cause the U.S. to maintain relationships, which may not be in our best interests, in order to secure fuel sources.

To meet global energy demand without contributing to the increasing $CO_2$ problem, renewable energy options should be investigated. An ideal renewable energy option is one that is both economical and reliable in comparison to fossil fuels. Currently there are many potential renewable energy options, however, no single option has the capacity to approach the energy produced by fossil fuels.[5]

## 1.2 Potential Technologies for Renewable Energy

### 1.2.1 Wind power

A wind turbine is a simple method for converting the energy of the wind into electricity. Typically, a gearbox turns a slow moving turbine rotor into faster-rotating gears, which converts mechanical energy to electricity in a generator.[5] Wind farms generate electricity with little impact on the surrounding environment. In principle, winds above 100 m in altitude are capable of producing 1500 TW of electrical power. Wind power can generate a significant amount of power in feasible

locations; however, it cannot meet the total energy demand due to lack of suitable wind power locations. [5]

### 1.2.2 Hydroelectric energy

Hydroelectric energy is an attractive renewable energy resource that harnesses the kinetic energy of falling or moving water to turn an electric turbine. Currently hydroelectric dams produce 7% of the total electric power generated in the United States.[6] However, hydroelectric energy could never provide what the United States or the rest of the world requires due to limitations in the number of hydropower plant sites. Most hydropower sites that could provide significant power generation have already been developed. Harvesting hydroelectric power results in large environmental impacts that effect land use, homes, and natural habitats.[7]

### 1.2.3 Biomass

Production of electricity from biofuels and biomass has been increasing over recent years. Feedstock is produced by large-scale crop cultivation or through the use of microorganisms. Various crops such as corn and sugarcane are used to produce biofuels such as biodiesel, ethanol, and methane, which are then combusted to generate energy. In principal, this method of harnessing biofuel energy is carbon neutral in that the feedstock for the biofuels sequesters $CO_2$ as it grows and then releases $CO_2$ upon combustion. However, water, fertilizer, and other inputs used in the growing of crops generate carbon emissions. Biofuels currently do not provide adequate energy for the global energy demands. However, biofuels show potential

to replace petroleum as a liquid fuel source.[8] Biofuel feed stock requires a significant amount of land use, which would result in reduced biodiversity, deforestation, and competition of potential land that would be used for food production.[9]

### 1.2.4 Geothermal energy

Historically, in certain locations steam and hot water from below the earth's surface has been used to provide heat for buildings, industrial processes, and to generate electricity in geothermal power plants. Harvesting process have been estimated to be able to produce 70 to 140 GW, which lies well below today's current energy demands.[5] Geothermal energy is environmentally friendly, but may only be utilized in certain areas near geothermal hotspots. Harnessing geothermal adds an attractive approach to helping meet the global energy demands of 2040.

### 1.2.5 Solar energy

The entire global energy demand for 1 year could be satisfied if we were to capture all the light that hit the earth for just 1 hour.[10] If we were able to capture just a small proportion of that light we could satisfy current and future global energy demands.

Despite the desirable potential that solar energy offers, there are several reasons why solar energy has not contributed significantly to the energy market. The intermittency of solar power has proven to be problematic as solar power can

only be harnessed during daylight hours; evenings and darker days that follow towards the end of the year prove to be troublesome in harnessing solar energy.

In addition, solar energy is substantially more expensive than fossil fuels. The price of electricity produced from natural gas is between 5-7 cents per kWh, that for coal is between 4-10 cents per kWh, and from wind is between 4-10 cents per kWh.[11] The price of power generated from sunlight using a conventional PV cell over a 25 to 30 year lifetime is currently around 18 cents per kWh, which is nearly quadrupling the price of natural gas.[12]

## 1.3 Solar Concentration

### 1.3.1 Conventional designs

A number of strategies are being investigated aimed at reducing the cost of solar power. One approach is to employ solar concentration. Increasing the energy flux by the means of solar concentration is an attractive approach to reducing the cost of solar energy.

A Fresnel lens focused onto a photovoltaic (PV) cell is one approach in concentrating light for the use of electricity (Fig 1.3). The Fresnel lens concentrates light like a traditional convex optical lens, but with a reduced amount of material required. The result of the Fresnel lens is a thinner and flatter surface that allows the capture of more oblique light from a light source. Fresnel lenses have concentration ratios of up to 250x.[13] The Fresnel lenses however are limited by their small acceptance angles. [14]

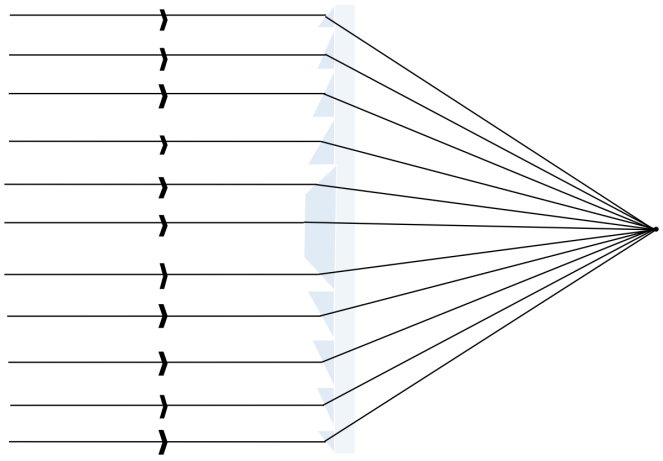

Figure 1.3 Cross-sectional view of a Fresnel lens.[13]

These small acceptance angles would be problematic in practical applications due to the Suns' non-stationary position and require expensive solar tracking.

A solar power tower is another type of concentrator design. The solar power tower is a large area thermal concentrator that reflects sunlight off sun-tracking mirrors, termed heliostats, that in turn focus the sun's rays upon a collector tower. Heat exchangers are placed at the collector tower, which utilize steam or molten salts for power generation (Fig 1.4). Solar power towers can achieve concentration ratios greater than 1500x and in addition have the potential to operate over a 24-hour period by heating the steam drum. However, solar power towers require a substantial investment in materials and land use.[15]

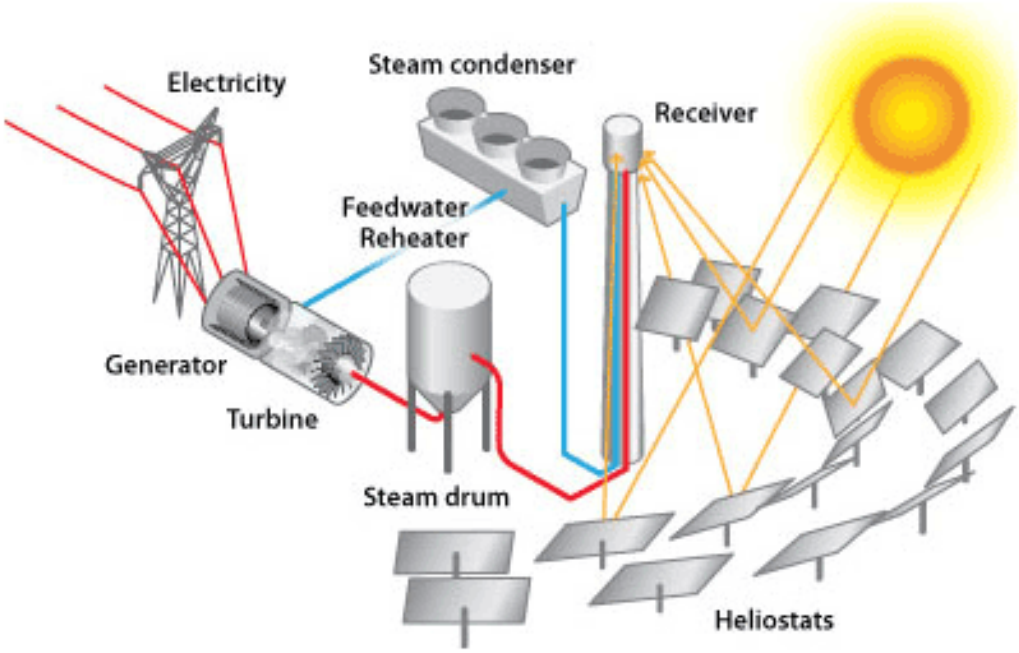


Figure 1.4 Diagram of a solar tower power plant.[15]

Parabolic trough arrays represent another type of a solar thermal concentrator. The concentrators use a parabolic mirror that focuses light to a focal line. Along the focal line a receiver pipe is filled with a working fluid where heat is then exchanged for power generation (Fig 1.5). Solar tracking technology produces a concentration ratio of 100x, with an energy conversion efficiency ranging from 24-26%.[15] This method is relatively simple in design, but is relatively high cost due to expensive solar tracking.

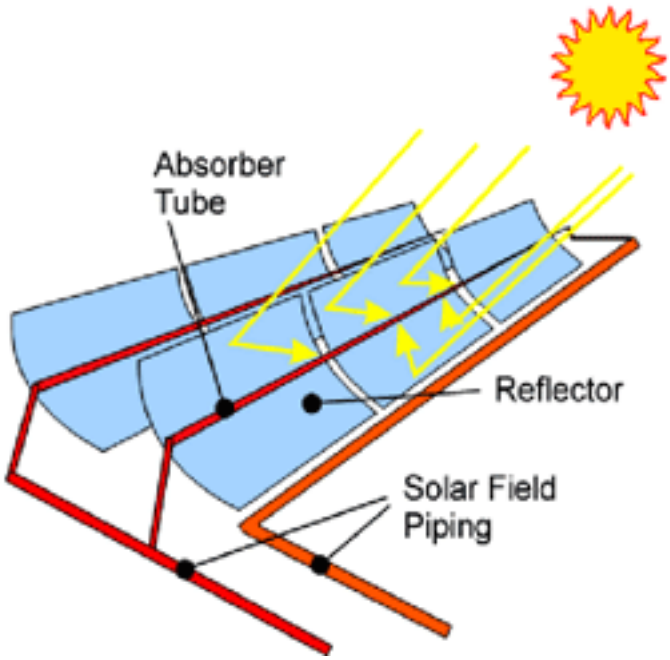


Figure 1.5 Diagram of parabolic trough.[15]

A solar dish is a comparable method to that of the solar power tower, and parabolic trough. A dish is mounted to a tracking structure that follows the sun periodically through the day. The resulting energy from the sun is reflected onto a receiver that collects the solar thermal energy (Fig 1.6). Solar dish technology produces relatively small amounts of electricity compared to other solar conventional designs, typically in the range of 3 to 25 kilowatts.[16] The lower energy output compared to other solar conventional designs inhibit the solar dish from being a practical concentrator in the solar energy market.

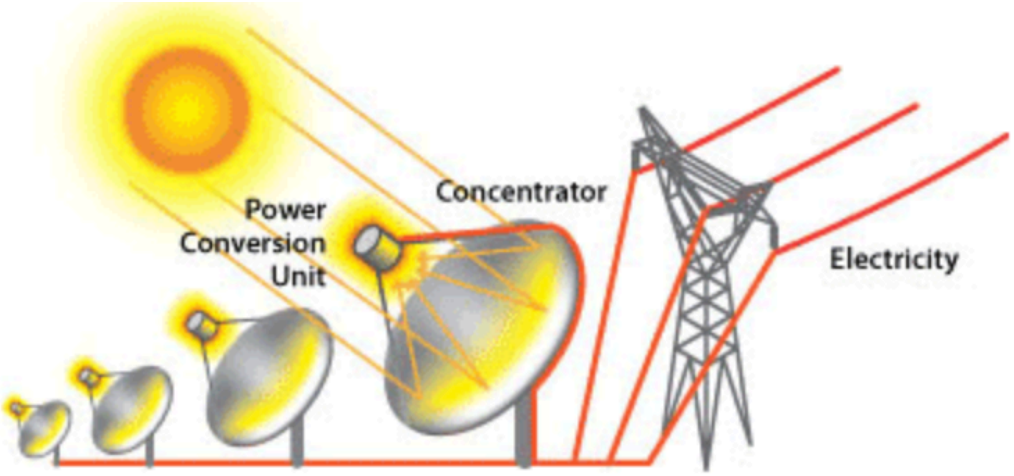


Figure 1.6 Diagram of solar dish plant.[16]

### 1.3.2 Low-gain concentrators

Another strategy in solar concentration is to employ a low-gain design. A low-gain design system concentrates light in the range of 2-100x. These types of concentrators are lower in cost, have a high acceptance angle, and do not require solar tracking due to their high acceptance angle.[17]

Plasmonic nanoparticles such as silver, gold, and copper have been coupled to thin-film solar cells.[18] The nanoparticles improve the absorption cross-section of these solar cells by minimizing the amount of light reflected or transmitted through the interface. These plasmonic structures can reduce the physical thickness needed in semiconductors in three ways. The first is caused by the nanoparticles acting as subwavelength scattering elements that couple and trap photons from the sun into the semiconductor thin film (Fig. 1.7 A.). The second is caused from the particles acting as antennas in which the plasmonic energy is coupled to the semiconductor

thus increasing its effective absorption cross-section (Fig 1.7 B.). The third is the coupling of light into surface plasmon polaritons propagating at the metal/semiconductor interface (Fig 1.7 C.).[19] However, this technique has proven troublesome in large scale applications due to plasmonic coupling effects, which require integration of dense array of metal nanostructures that need low tolerances at the nanometer scale.[19]

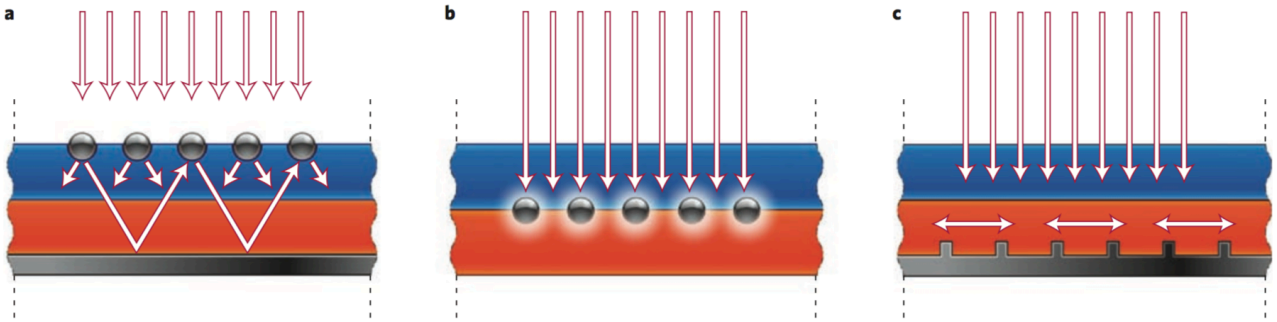


Figure 1.7. Plasmonic light trapping geometries. Reproduced with permission from author.[19]

## 1.4 Summary

With the increasing demand in global energy use and the rise of global atmospheric $CO_2$ levels it has become evident that renewable energy must increase to represent a larger share of future energy production. Solar energy currently represents a minor contributor to the global energy market; however, in principle solar has the potential to meet all the worlds' energy demands. Solar concentrators have been able to achieve large concentration ratios, but suffer in power conversion, reliability, and cost as compared to other energy options.

# Chapter 2: Luminescent Solar Concentrators

## 2.1 Introduction to Luminescent Solar Concentrators

In the 1970's luminescent solar concentrators (LSCs) were first proposed as a means of reducing the cost of solar generation by the reduction of photovoltaic (PV) area.[20-22] An LSC consists of a wave guiding material, which is typically made from glass or plastic that contains a luminophore. The luminophore absorbs a certain portion of the solar spectrum, which is then re-emitted and trapped by the host matrix through total internal reflection (TIR). The trapped light can travel through the wave-guided material until it reaches an edge where a thin strip PV is placed in order to capture that light and convert it into electricity (Fig 2.1).[20-24]

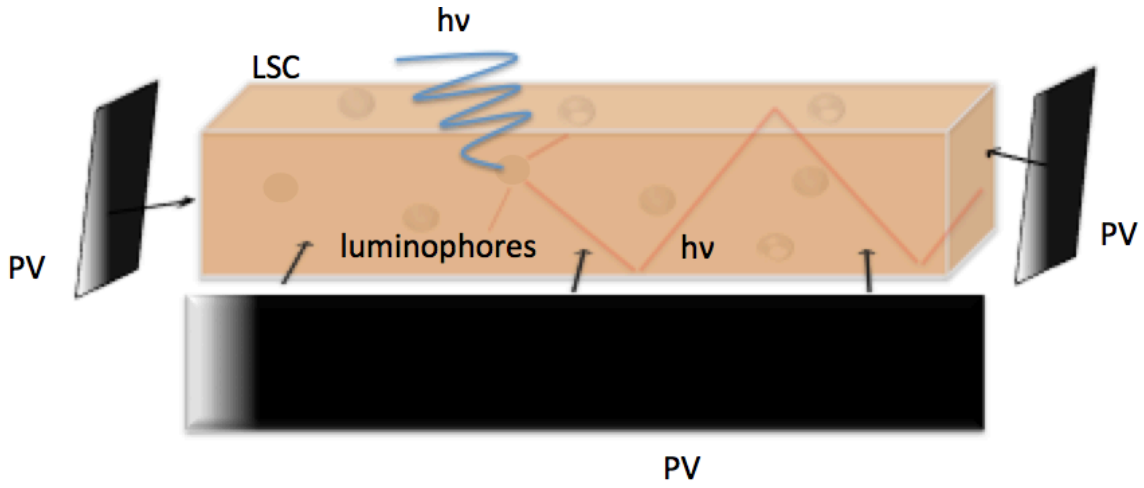


Figure 2.1 A luminescent solar concentrator.

A high concentration ratio is obtained by placing thin PV strips along the edges of a two-dimensional LSC. The concentration ratio (CR) is defined as the ratio

between the power per unit area of incident sunlight to the power per unit area of concentrated light. As the CR of a concentrator increases the price per peak watt decreases because the concentrator is providing more power per unit area. The CR for an LSC is related to the geometric gain, G, for an LSC. G is defined as the ratio of the facial surface, $A_{face,}$ to the total area of the concentrators' edge, $A_{edge}$.

$$G = \frac{A_{Face}}{A_{Edge}} \qquad \text{(Equation 2.1)}$$

A common metric for expressing the efficiency of light concentration is the optical quantum efficiency (OQE). OQE is defined as the fraction of absorbed photons, $n_{abs}$ , that reach an edge concentrator, $n_{edge}$:

$$OQE = \frac{n_{edge}}{n_{abs}} \qquad \text{(Equation 2.2)}$$

CR, G, and OQE are useful metrics in describing efficiency and performance of LSCs. These terms will be used throughout this thesis to assess and describe LSC performance.

## 2.2 Design advantages

The key advantage of LSCs is their ability to concentrate both direct and diffuse radiation, along with the potential to make them partially transparent. Consequently, LSCs do not require expensive tracking systems to follow the path of the sun.[25] The LSC allows for omnidirectional acceptance of light, which enables comparable performance under diffuse or direct illumination. LSCs also possess the potential for higher CRs than conventional design solar concentrators.[26] This type of

concentration can open new avenues to improving solar conversion efficiency, scalability, and cost by providing high brightness, narrow-bandwidth light optimized for PV or photochemical conversion. These features make LSCs applicable to northern latitudes and also suitable for building integration, such as transparent solar windows.

## 2.3 LSC device performance

During 30+ years of development, LSCs have yet to make a practical impact in the solar power market.[27] This can be attributed to the lack of suitable luminophores and the reduction of the optical efficiency as the concentrator increases in size. [28] The theoretical thermodynamic CR limits of $10^4$x – $10^5$x are not observed for current LSCs. The current highest reported achievable concentration ratios have been ≤ 10x.[29] For LSCs to make an impact in the energy market a CR of $10^2$x – $10^3$x would need to be achieved. [30, 31]

In addressing the efficiency of an LSC, it can be rather difficult to compare devices reported by different groups due to large variations in LSC design, materials, and testing methods. However, an effective method of comparison of LSC device performance is the optical power efficiency (OPE). OPE is defined as the percentage of incident solar power concentrated by the LSC.

$$OPE = \frac{OQE * \int_{AM\ 1.5} Abs. * E_{Edge\ Photon.}}{1000\ \frac{W}{m^2}} \qquad \text{(Equation 2.3)}$$

Where the optical quantum efficiency (OQE) defined previously, represents the percentage of absorbed solar photons reaching an LSC edge, and $E_{Edge\ Photon}$ represents the energy of the photons emitted at the edge.

In the past, concentrators have been compared by external quantum efficiency (EQE), defined as the fraction of incident photons (AM1.5 G solar spectrum), $E_{Incident\ Photons}$, converted to electrons produced by the PV cell, $E_{LSC}$.

$$EQE = \frac{E_{LSC}}{E_{Incident\ Photons}} \qquad \text{(Equation 2.4)}$$

However, the EQE comparison for LSC performance is highly dependent upon the quality of the PV cells chosen. It is more beneficial to compare the OPE as the power conversion efficiency is specific to the LSC itself.

## 2.4 Light propagation and loss

We must first understand how light propagates through an LSC in order to understand the factors limiting device performance. The concept of an LSC is rather easy to understand, but the detailed mechanisms of light propagation are rather complex. A certain proportion of incident solar photons will be reflected back, which is known as front face reflection. Typically, about 4% of incident photons will be reflected while the other 96% will penetrate into the waveguide. Inside the LSC host matrix a proportion of photons will pass through based on the optical density (OD) of the LSC. Another proportion of photons will be lost due to the energy mismatch between the light and the luminophores' energy band gap. The proportion of

remaining light may be absorbed and reemitted by a luminophore, which would then be determined by the luminescence quantum yield, QY:

$$QY = \frac{Photons\ Emitted}{Photons\ Absorbed} \qquad \text{(Equation 2.5)}$$

The emitted photons from the luminophore have a certain probability of being emitted within an escape cone as well as a probability of being emitted at an angle outside of the escape cone (Fig 2.2). Photons emitted outside of the escape cone are trapped by total internal reflection (TIR). These photons will travel to the edge of the LSC by TIR unless they are reabsorbed by another luminophore, absorbed by the matrix, scattered from surface roughness, or scattered by another particle. The remaining photons will have a certain probability of generating a photocurrent in an edge-attached PV.

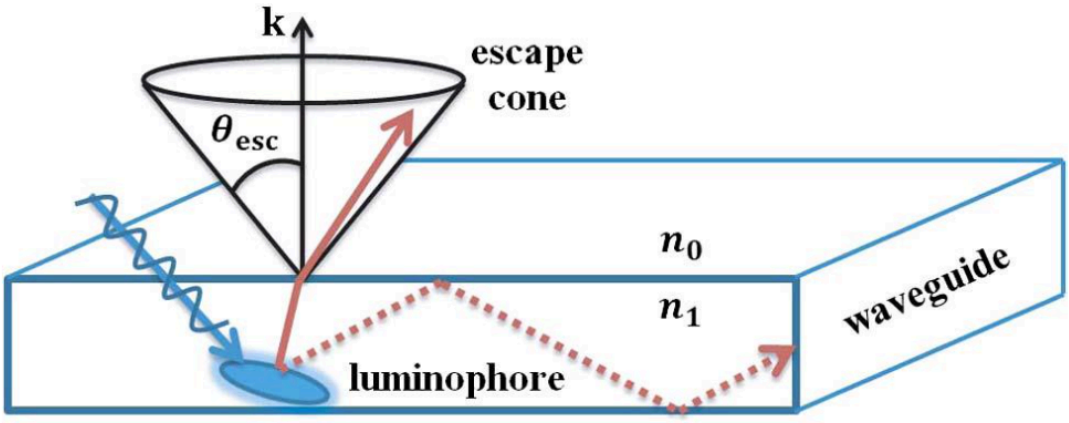


Figure 2.2 Light propagation through an LSC.

### 2.4.1 Refraction

Snell's law describes what happens to light traveling between media with different refractive indices.

$$n_1 \sin\theta_1 = n_2 \sin\theta_2 \qquad \text{(Equation 2.6)}$$

As light travels from a medium with a refractive index ,$n_1$, to another medium with a refractive index of $n_2$, it is refracted at an angle of $\theta_2$ .

### 2.4.2 Total Internal Reflection

At a certain angle the probability of reflection will be 100%, which is known as the critical angle, $\theta_c$, defined as

$$\theta_c = \sin^{-1}\frac{n_2}{n_1} \qquad \text{(Equation 2.7)}$$

As an angle of incidence increases away from $\theta_c$, there will be a greater probability that a reflection will occur at the interface between the two media. This phenomenon only occurs when the light travels in the medium with the higher refractive index.

### 2.4.3 Escape cone

The critical angle also defines an escape cone for a photon emitted within an LSC. An angle less than or equal to $\theta_c$ (equation 2.7) light will escape the waveguide. Rotating $\theta_c$, $360^0$ about an axis normal to the face of the medium creates an escape cone, defined as equation 2.8. [32]

$$\varphi_{cone} = 2\pi(1 - \cos\theta_c) \qquad \text{(Equation 2.8)}$$

A luminophore embedded within the LSC will emit photons isotropically so a certain fraction will be lost out the front and bottom face of the LSC. Substituting equation 2.7 into equation 2.8 and then simplifying, a relationship is defined giving the probability a photon is lost to the escape cone (Equation 2.9).[25]

$$P = 1 - \sqrt{1 - \frac{1}{n_1^2}} \qquad \text{(Equation 2.9)}$$

A polymer wave-guide made with a high refractive index material such as PMMA (1.5), corresponds to a total probability, P, of 25% lost through the escape cone. The remaining 75% of the photons are trapped by TIR, which are guided to the edges of the LSC to be collected by a PV.

### 2.4.4 Surface Scattering

An escape cone loss is just one of several mechanistic losses possible in the waveguide. A photon can also be lost at the surface of an LSC due to scattering from surface roughness. The surface roughness can refract and reflect photons out of the waveguide at each interface. The loss rate due to surface roughness can be approximated by the following equations:[33]

$$\alpha_s = K^2 * \frac{cos^3(\theta_m)}{2\sin(\theta_m)} * \frac{1}{(t_{waveguide})} \qquad \text{(Equation 2.10)}$$

$$K = \frac{4\pi}{\lambda} (2\sigma^2_{waveguide})^{1/2} \qquad \text{(Equation 2.11)}$$

where $\alpha_s$ is the attenuation losses due to surface scattering $cm^{-1}$, K is a unit-less quantity that defines all the surface properties of the waveguide, $\theta_m$ is the angle of the incident photon normal to the surface of the LSC, $t_{waveguide}$ is the LSC thickness, and $\sigma_{waveguide}$ is the mean surface roughness of the LSC. Surface scattering can be the dominating factor in photon losses for thin LSCs. When a large number of reflections is required to reach an edge.

### 2.4.5 Light scattering from particles

Particles near or above the wavelength of light are capable of scattering light that interacts with them. Rayleigh scattering models this type of particle scattering, which is dependent upon the size of the particle and the wavelength of light being scattered,[34]

$$\sigma_1 = \frac{8\pi r^6}{3}\left(\frac{2\pi}{\lambda}\right)^4\left[\frac{n_{np}^2 - n_{poly}^2}{n_{np}^2 + 2n_{poly}^2}\right]^2 \quad \text{(Equation 2.12)}$$

$$\alpha_s \approx \frac{3\rho\sigma_1}{4\pi r^3} \quad \text{(Equation 2.13)}$$

where $\sigma_1$ represents the scattering cross-section for a single particle scattering event, $\lambda$ is the wavelength of light, r is the radius of the particle, and n is the refractive index of the medium. Equation 2.13 represents the total light scattering due to particles for an LSC, where $\rho$ represents the particle volume fraction and $\alpha_s$ ($cm^{-1}$) is the loss rate. Since the momentum vector of light changes once scattered off a particle, there exists a probability that a scattered photon will escape the waveguide and become lost.

LSCs based on molecular compounds such as organic and inorganic dyes are not typically affected from particle scattering due to their size being much smaller then the wavelength of light. However, LSCs based on nanocrystal technology such as quantum dots are prone to aggregation creating larger particles capable of scattering light.

### 2.4.6 Matrix absorption

Very little absorptivity occurs from the matrix materials typically used in LSCs (e.g. poly (methyl methacrylate)). What little there is can be attributed to impurities in the matrix itself, such as additives or remaining initiator. In addition, as an LSC becomes larger in geometric size the chance of overtone absorptions from the matrix becomes more prominent.[25] However, overall matrix absorption typically accounts for very little of the LSC attenuation.

## 2.5 Material Optimization for LSCs

### 2.5.1 Waveguide Matrix

To increase LSC performance, the LSC matrix should have a high optical clarity, be environmentally stable, and have a high refractive index. Optical clarity is important due to the long propagation lengths that photons will travel in an LSC, which can exceed a meter. LSCs used outdoors need to be able to tolerate harsh weather conditions in addition to prolonged UV light exposure. PVs have now become more robust with an extended life-time up to 30 years; an LSC would need to be designed to last as long as the PV in order to make the system effective from a manufacturing stand point. Lastly, the material would need to have a high refractive index in order to reduce the size the escape cone.

Very few materials have been able to meet these criteria. Glass possess high optical clarity with a complementary high refractive index, but suffers in manufacturing and cost due to the high processing temperatures, which will degrade most luminophores. Most LSC research for the last 10 years has been

focused on polymer waveguide materials. Polyvinyl alcohol, poly(methyl methacrylate) (PMMA), and poly carbonate derivatives have been the top choices for researchers due to their ability to meet the above criteria.[35, 36] PMMA and its derivatives is the most common choice for most researchers as a waveguide material.[23, 29, 37]

### 2.5.2 Luminophores

Luminophores are as important as the waveguide material itself. In order to create an effective LSC, the luminophore needs to be low cost, photostable, posses a high quantum yield, absorb a large portion of the solar spectrum, and have a relatively large Stokes-shift. The luminophore needs to be cost effective in order to drive down the price. The luminophore will be bombarded continuously with UV light and must be able to resist degradation and last as long as the PV cells. It is crucial that the luminophores have a high quantum yield because it determines the probability that a photon absorbed will be re-emitted. The luminophores must be able to absorb a large portion of the solar spectrum because a larger collection of the solar spectrum increases the probability of generating more photons, thus increasing the OPE and CR. A large effective Stokes shift decreases the overlap between the absorption and emission spectra of a luminophore. The greater the overlap between the absorption and emission in a luminophore the greater chance that a photon emitted from a luminophore will be reabsorbed and lost out the escape cone or to a non-radiative pathway (section 2.4).

### 2.5.3 Organic Dyes

Organic dyes have been thoroughly investigated since LSCs were first conceived. Their low cost and compatibility with a polymer matrix are two of their advantages. The molecular structure of organic dyes is based on a π-electron conjugated system.[25] Their absorption and emission spectra can be tailored by changing the π-electron system via molecular structure.[38] Organic dyes have shown promise in small LSC applications due to their high chemical stability and luminescent quantum yields reaching above 95%. However, in larger scale applications their performance drops substantially, due to a small Stokes-shift between the absorption and emission band. A small Stokes-shift results in a high probability emitted light will be reabsorbed by neighboring luminophores inside the concentrator and eventually lost through emission via the escape cone.[39]

### 2.5.4 Quantum Dots

Quantum dots (QDs) are luminescent semiconducting nanocrystals that are typically a few nanometers in size. As the bulk semiconducting crystal is reduced to the nanometer scale, it begins to exhibit quantum properties. At the nanoscale the QD will become smaller than the natural radius of its electron-hole pair, known as its characteristic Bohr radius. When this happens the electron-hole pair becomes confined altering the bandgap. The size of the nanocrystal changes the confinement energy, which allows tunable spectral properties.[40, 41] Quantum dots show promise as being an effective luminophore with high photostability, broad solar absorption,

and quantum yields that exceed 85%.[42] However, their small Stokes-shift hinders their effectiveness in large-scale LSC applications.

## 2.6 Summary

LSCs have the potential to further reduce the overall cost of renewable energy production. The major obstacle for LSC commercialization is the ability to find a suitable luminophore that satisfies the aforementioned performance criteria. Reabsorption losses are found to be the major dominating loss factor as an LSC grows in size. The ideal luminophore would have little overlap between the absorption and emission bands, absorb a large portion of the solar spectrum, have a near unity quantum yield, and output narrow-bandwidth light optimized for PVs.

# Chapter 3: Doped Quantum Dot Luminescent Solar Concentrators

A number of approaches have been investigated to mitigate the overlap between fluorphore absorption and emission spectra. Researchers have attempted to control the orientation of luminophores in order to increase light being emitted in waveguided modes[43-46], applied dichroic mirrors to the LSC to block emitted light out the escape cone[47, 48], and utilized large Stoke-shift luminophores.[37, 49]

A new type of luminophore has been investigated that involves impurities or native defects in the QDs  such materials are sometimes called doped QDs, show a large separation between their absorption and emission bands.[23] In addition, doped QDs absorb strongly over a broad range of the solar spectrum without sacrificing efficiency in QY or photostability.[29] Doped quantum dots can be made from low cost, non-toxic, earth abundant materials that have high compatibility for integration into LSC applications.

## 3.1 $Mn^{2+}$ Doped Quantum Dots

For this this section we will focus on $Mn^{2+}$ ZnSe Quantum dots. ZnSe selectively absorbs from the ultraviolet to part of the visible blue spectrum. This preference of absorption is due to ZnSe being a direct bandgap semiconductor with a bulk bandgap of ~3.1eV. The ZnSe lattice provides a weak tetrahedral field, where an $Mn^{2+}$ ion can replace a $Zn^{2+}$ ion within the crystalline lattice.  The $Mn^{2+}$ impurity in the host lattice introduces new electronic state into the ZnSe QD.

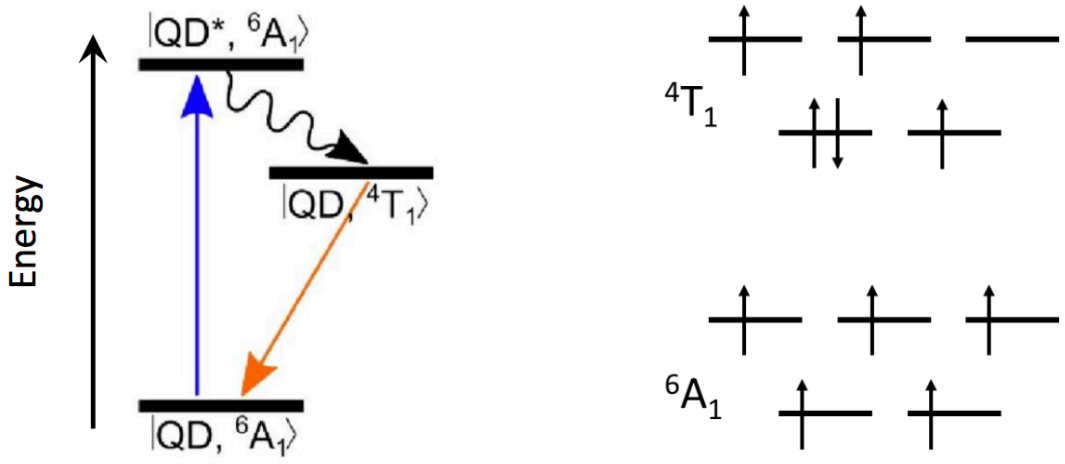


Figure 3.1 Photophysical diagram of $Mn^{2+}$ doped ZnSe quantum dots.[23]

The tetrahedral field of the $Mn^{2+}$ ion posses a $^6A_1$ ground state that has a luminescence associated with a $^4T_1$ to $^6A_1$ d-d transition at an energy of ~2.1 eV (figure 3.1).[23, 50] When a photon is absorbed from the bulk band gap of ZnSe, an electron hole pair is created, and the energy of the exciton is transferred to $Mn^{2+}$, which causes a spin flip in the d-orbital electron configuration producing the $^4T_1$ excited state. This promotion is only feasible due to its energy level lying below the conduction band of the ZnSe host lattice. This energy transfer process occurs on the order of picoseconds, which greatly exceeds the rate of exciton recombination of nanoseconds.[51] The energy transfer is thus favorable from the host ZnSe lattice to the $Mn^{2+}$.

The spin transition from the $^6A_1$ to $^4T_1$ is spin-forbidden, with an extinction coefficient of ~1 $M^{-1}$ $cm^{-1}$, 5 orders of magnitude smaller than that of the host nanocrystal. The difference in absorbtivity between the $Mn^{2+}$ and the host nanocrystal yields a large effective Stokes shift of ~1 eV, eliminating overlap

between the absorption and emission band. These quantum dots showed great promise in LSC applications, however, they suffer from poor efficiency due to their small absorption of the solar spectrum.

## 3.2 $Cu^{2+}$ CdSe Quantum Dots

Copper-doped semiconductors played a central role in the development of lighting and display technologies during the 20$^{th}$ century. This development has lead to an understanding of their spectroscopic, chemical, and physical properties.[52] Doping with copper replaces $Cd^{2+}$ with $Cu^{2+}$ in the host crystalline lattice giving a structural composition of $Cu_xCd_{1-x}Se$. The introduction of copper into the host lattice creates an intermediate energy state that lies slightly above the valence band. This state allows for a further Stokes shift with a tunable emission in the NIR. Photoluminescence emission occurs primarily from localized paramagnetic states in the bandgap produced by hole transfer to $Cu^{+}$ from the photoexcited nanocrystal (figure 3.2).[53, 54] The hole transfer from the valence band to the $Cu^{+}$ energy gap state is fast and efficient, leading to a large effective Stokes shift.

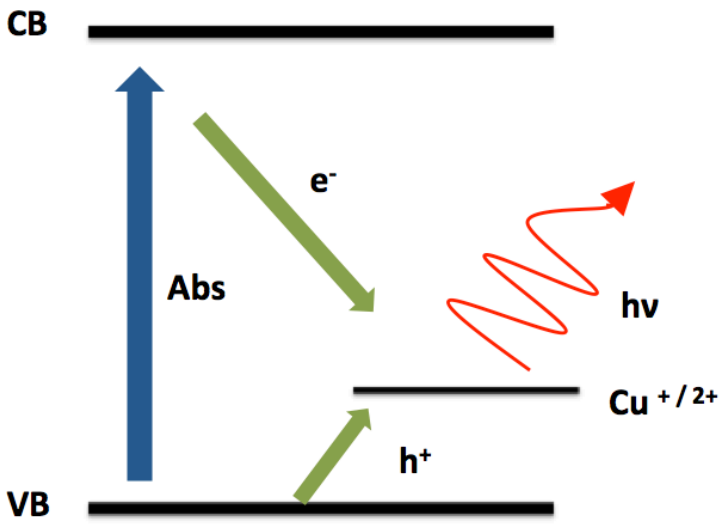


Figure 3.2 Photophysical diagram of $Cu^{+}$ doped CdSe quantum dots.[55]

The QY for $Cu^{+}$ doped CdSe is relatively low compared to other QDs with QY's ranging from 20-40%. Even with a low QY, $Cu^{+}$ doped CdSe outperforms competitors such as CdSe/CdS, CdSe/CdS dot-in-rod, and $Mn^{2+}$ doped QDs in large scale LSC applications.[55] Their higher performance stems from a large cross-sectional absorption with relatively small reabsorption losses. These QD's show potential for LSC applications; however, a QD with a higher QY would mitigate reabsorption losses through increased photon recycling in larger scale LSC applications.

## 3.3 Copper indium disulfide quantum dots

Different types of luminophores have been researched for LSC applications, but many luminophores have been found not suitable due to reabsorption losses, small solar spectrum absorption, and low QY. This thesis introduces a new type of luminophore, copper indium disulfide (CIS) quantum dots to be used in LSC

applications. This luminophore exhibits interesting properties that are similar to those of doped QDs with regards to a relatively large Stokes shift and high luminescent QY; however, the copper is part of the host lattice itself and is not a dopant. The CIS luminophore exhibits photophysical properties that are similar to those of $Cu^{+}$ doped CdSe QDs (figure 3.2). CIS QDs can be synthesized in large quantities without the need of expensive precursors and can be made to contain no heavy metals.[56]

These luminophores posses a large effective Stokes shift (~500 meV), a relatively small bulk band gap (~1.5 eV) and a high luminescent QY (~86%).[29, 57, 58] CIS QDs show the potential to outperform other luminophores in regards to large-scale LSC applications and will be the focus of this thesis.

# Chapter 4: Experimental Methods

## 4.1 CIS QD Synthesis

CIS QDs were synthesized in a two-step process following literature methods.[56-58] The first step of the synthesis is the growth of the crystal core. The CIS ternary nanocrystals were prepared by adding equal molar indium acetate (0.292 g, 1 mmol) and copper (I) iodide (0.190 g, 1 mmol) to excess 1-dodecanethiol (DDT, 5 mL) in a three-necked flask. The solution was stirred vigorously and degassed 3 times by a pump/purge method. The solution was kept under nitrogen and raised to 100 $^{0}$C to form the CuI, $In(Ac)_3$ , and DDT intermediate complex. The solution was held at 100 $^{0}$C until all precursors were dissolved and a transparent yellow solution was formed. The temperature was raised and held at 205 $^{0}$C. At this temperature the formed complex decomposes into CIS nanocrystals. After 20- 120 minutes, depending on desired size, the nanocrystals were cooled back down to room temperature.

The CIS nanocrystals cores have a relatively low photoluminescent QY that ranges from 5-10%. The photoluminescent QY can be increased by the growth of a shell around the core. This secondary crystalline growth passivates surface defects where the charge carriers can be come trapped or relax non-radiatively. The inorganic passivation layer is created in several steps.

The first step in the inorganic passivation layer is the synthesis of cadmium myristate. Sodium hydroxide (0.12 g, 3 mmol), myristic acid (0.6 g, 2.63 mmol), and methanol (30 mL) were added to a 100 mL round bottom flask and sonicated with heat (55 $^0$C) until dissolved. Cadmium nitrate tetra-hydrate (0.308 g, 0.998 mmol) and methanol (5 mL) were added to a separate 50 mL round bottom flask and sonicated until dissolved. The cadmium solution was added dropwise to the myristate solution forming the precipitant cadmium myristate. The cadmium myristate was dried overnight.

The second step is the creation of a colloidal solution that contains the reagents to promote shell growth. Cadmium myristate (0.227 g, 0.4 mmol) and elemental sulfur (0.013g, 0.4 mmol) was added to octadecene (4 mL) and sonicated for 1 hour at 60 $^0$C. The colloidal solution was pumped and purged 3 times and stored under nitrogen.

The inorganic passivation layer of the CIS QD cores is achieved by taking an aliquot of the CIS core solution (1 mL) and adding octadecene (5 mL) to a 3-neck round bottom flask. The CIS core QD solution was stirred vigorously and degassed 3 times by a pump/purge method. The solution was raised to 180 $^0$C to promote nucleation of the secondary crystalline layer around the nanocrystals. At 180 $^0$C the colloidal cadmium myristate/sulfur solution was added via hot-needle injection at a rate of 12 mL*hrs$^{-1}$ (figure 4.1). The solution was cooled down to room temperature after all 4 mL of colloidal solution was added. During the cooling process at ~90 $^0$C,

oleic acid (0.1 mL) was added as excess ligand for helping further to suspend the QDs in solution.

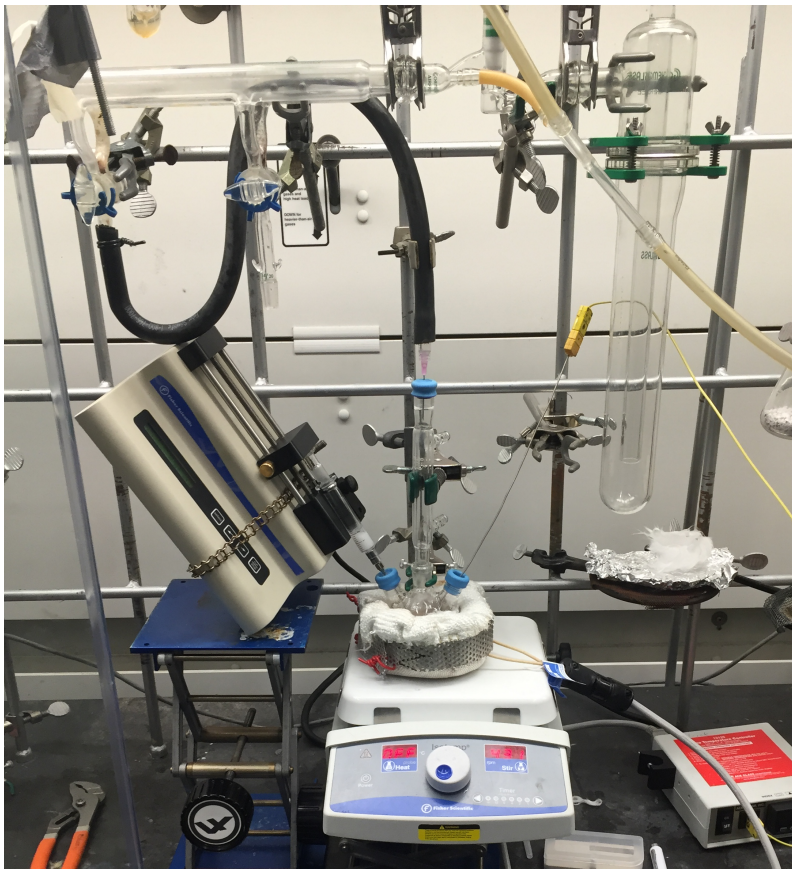

Figure 4.1 Experimental setup of shell growth for CIS QDs.

The CIS QDs, now with a cadmium sulfide shell, were purified by centrifugation. An aliquot of CIS QDs (~1.5 mL) was added to toluene (1 mL) and excess ethanol. The toluene and ethanol forms an azeotrope, allowing for the removal of unreacted reagents and byproducts. The CIS QDs are however not soluble in the solution and crash out forming precipitated pellets at the bottom. The centrifuged solution was decanted and the CIS QD's were re-suspended in toluene. (Note. This synthesis was carried out at Western Washington University; however,

most of the QDs used to construct devices were sourced from our collaborators in Prof. Daniel Gamelin's group at the University of Washington, who use similar methods.)

## 4.2 Relative Quantum Yield.

Quantum dots need to have relatively high quantum yield in order to be effective luminophores for LSC applications. To determine the QY of the QDs, another luminophore with a known QY is used as the reference. Toluene (3 mL) was added to a pair of the quartz cuvettes. The reference dye chosen was Lumogen Red (BASF) due to a well-known QY and an overlap of absorption and emission with the CIS QD's (figure 4.2). To one of the cuvettes CIS QDs were added until an optical density (OD) of 0.1 was obtained. To the other cuvette Lumogen Red was added until an OD of 0.1 was obtained. The optical density at 475 nm for both samples was obtained using a Jasco UV-Vis 670 instrument. The emission was collected for both samples using a Horiba Fluorolog-3 double monochromatic fluorometer.

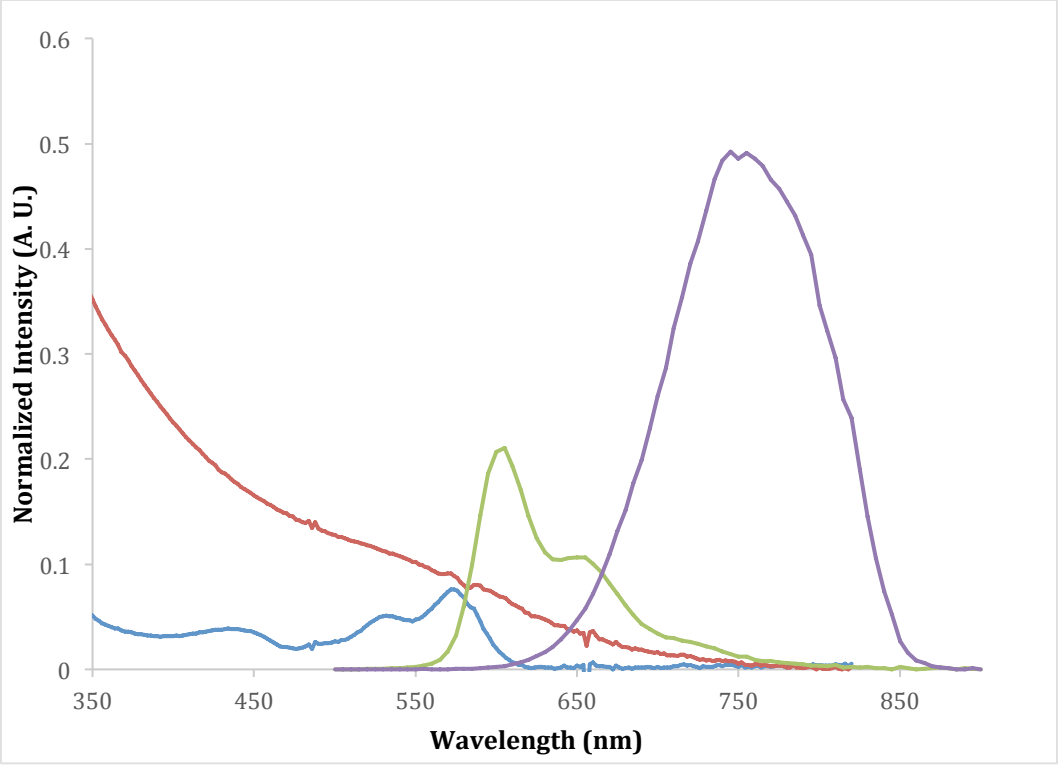


Figure 4.2 Normalized emission and absorption of Lumogen red and CIS QDs.

From Figure 4.2 the broad purple emission is that of CIS QDs, the sharp green emission is Lumogen red, the broad red absorption is CIS QDs, and the blue absorption is that of Lumogen red. Integrating the intensity of the emission and absorption for both sample and reference will allow for the determination of the relative quantum yield using equation 4.1.

$$QY = \frac{Emission_{samp}}{Emission_{ref}} * \frac{Abs_{ref}}{Abs_{samp}} * QY_{ref} \qquad \text{(Equation 4.1)}$$

## 4.3 Device Fabrication

### 4.3.1 Creating the Polymer Solution

Most LSCs have been fabricated using PMMA as the host matrix for embedding luminophores. PMMA meets the requirements for large-scale LSC applications, however the material is lacking compatibility with CIS QDs. PMMA is a relatively polar molecule and the interaction of the side chain is unfavorable with the non-polar myristic and oleic ligands of the CIS QDs. A derivative of PMMA, Polylauryl methacrylate (PLMA) provides the same optical properties as PMMA and has similar chemical properties. The difference between the two polymers is the side chain. PLMA has a 12 carbon long chain that is non-polar and is very similar to the ligands of the CIS QDs while PMMA has a side chain that is 1 carbon long. This difference in side chains results in a more favorable interaction between the polymer and the CIS QDs.

PLMA (MW 250,000) was dissolved into lauryl methacrylate (LMA) in a 1:3 ratio by weight. To the solution, Irgacure 651 photo-initiator (0.50 % wt.) and ethylene glycol dimethacrylate (2 % wt.) was added and homogenized overnight. LMA and ethylene glycol dimethacrylate were run through a silica column prior to the addition to the polymer solution in order to remove radical inhibitors added by the manufacturers.

Acrylates shrink roughly by ~10 % by volume upon polymerization causing delamination in the LSC. The delamination process causes the polymer to physically separate from the glass. A PLMA/LMA blend helps reduce the overall shrinkage of

the polymer matrix. Adding PLMA helps reduce the overall shrinkage upon polymerization.

### 4.3.2 LSC Shell

The LSC shell is a mold, which supports the polymer matrix with the embedded luminophores. In preparing an LSC shell, two pieces of 0.90 mm-thick B270 glass sheets (Howard Glass Inc.) were first cleaned by sonication in a 1% solution of Liquinox. The B270 glass sheets were air-dried and stored in a clean hood. To one side of each B270 glass sheet, 3-(trimethoxysilyl) propylmethacrylate was applied twice. The 3-(trimethoxysilyl) propylmethacrylate acts as an adhesion promoter to inhibit delamination. 3-(trimethoxysilyl) propylmethacrylate replaces the hydroxyl groups on the surface of the glass allowing the polymer to crosslink with the glass during the polymerization process. The treated glass was again cleaned to optical clarity.

To the treated side of the B270 glass sheets a transparent acrylic adhesive gasket (VHB tape, 3M Inc.) was cut to 4 mm thick strips and added to the surface around the edges forming a sealed cavity. The now empty shell was purged with nitrogen gas and stored for later use.

### 4.3.3 Determining the Amount of QD's

It is difficult to create an LSC made from CIS QDs with a desired concentration due to uncertainties in the concentration of QDs created during the synthesis. To create an LSC with a desired OD, an aliquot of CIS QD solution (20 uL) was diluted with toluene (3 mL) in a quartz cuvette. An absorbance spectrum of the

solution was taken using a Jasco UV-Vis 670 instrument. To determine the desired OD for a CIS LSC the following equations were used,

$$V_{QD\ Stock} = \frac{V_{total} * C_{LSC}}{\alpha * OD_{LSC} * OD_{QD\ Stock} * b}_{cuvette} \quad \text{(Equation 4.2)}$$

$$V_{premix} = V_{total} - \alpha * V_{QD\ Stock} \quad \text{(Equation 4.3)}$$

where α represents the volume fraction of QDs in a QD stock solution, $b_{cuvette}$ is the pathlength of cuvette used to measure the OD of the QD stock solution, $C_{LSC}$ is the thickness of the LSC, $V_{QD}$ is the volume of QD stock solution, $V_{premix}$ is the volume of LMA/PLMA/ethylene glycol dimethacrylate/irgacure 651 premix used, and $V_{total}$ represents the volume of filling solution after pulling off toluene.

### 4.3.4 CIS LSC

CIS QD stock solution was added to the polymer solution (section 4.3.1) and excess toluene from the QD stock solution was removed via vacuum. The CIS QD polymer solution was allowed to stir for at least 12 hours prior to polymerization to ensure a uniform mixing. The CIS QD polymer solution was injected into the LSC shell (section 4.3.2) and was immediately photopolymerized under uniform UV exposure for 1 hour. After polymerization, a transparent UV curing optical epoxy (n=1.56, Norland 63, Norland Products Inc.) was applied to the outer edges to give the LSCs smooth, optically clear edges. The completed LSCs for this work were 75 mm x 75 mm x 2.8 mm. The absorption for these LSCs encompasses nearly the entire visible spectrum, making the devices brown/red in appearance (Figure 4.3).

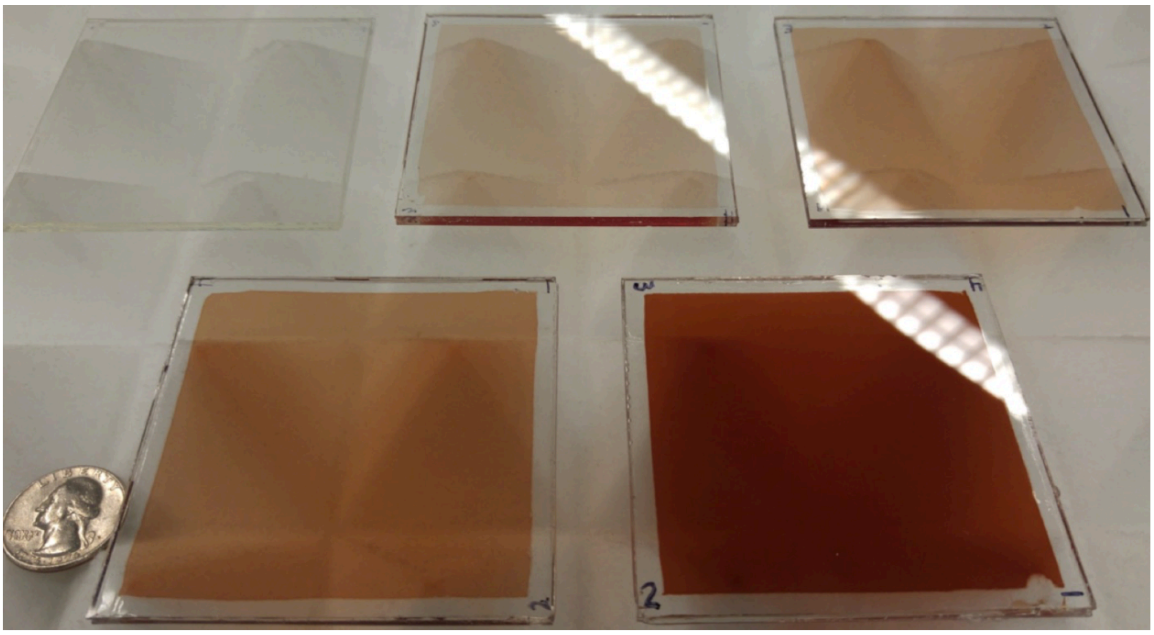

Figure 4.3 CIS QD LSCs presented in this work.

## 4.4 LSC Characterization

### 4.4.1 Measuring the LSC

The CIS LSC was excited by point illumination using a fiber optic bundle delivering monochromatic 475 nm light. The emission of the light coming out the edge of the LSC was monitored from 500-900 nm through an aperture of an integration sphere (Figure 4.4). The integration sphere was connected to another fiber optic bundle attached to a Fluorolog-3 double monochromatic fluorometer.

The illumination spot was varied in distance from the LSC edge. The integrated photon intensity from the emission spectrum was measured as a function of distance from the LSC edge. The remaining edges of the LSC device were blackened with black adhesive tape to eliminate any edge reflections. Fluorometer

emission response was calibrated in the wavelength range 500-900 nm using a reference dye 4-dimethylamino-4'-nitrostilbene in o-dichlorobenzene.[59]

Absorption spectra of the CIS LSCs were obtained by positioning the device in front of the solution cell mount so that the beam of light would pass through the face (1mm) of the LSC. Absorption was taken at multiple locations along the LSC to ensure the concentration and thickness remained constant. The absorption at different spots along the LSCs varied by <5% for all devices. All absorption measurements on LSC devices were taken using a Jasco V-670 UV-Vis.

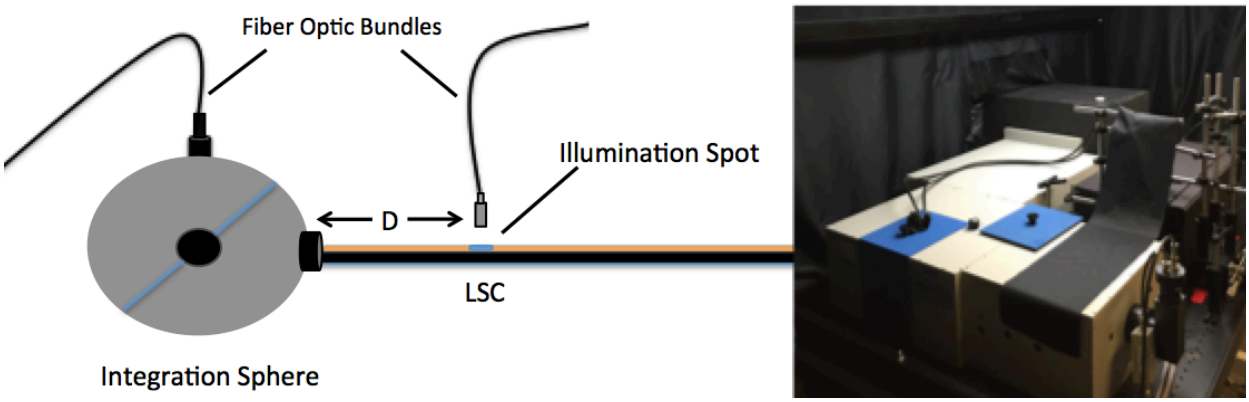


Figure 4.4 Experimental setup for measuring CIS LSCs.

### 4.4.2 Luminescent Spectrum Shift

A bathchromic shift (~80 meV) and a slight narrowing of the peak width was observed upon incorporation of CIS QDs into the polymer. This effect was observed in all samples including those with low OD. The excitation was measured as close to the edge of the LSC as possible for this measurement to minimize the optical path length and hence reabsorption caused changes to the spectrum. The shift results

from a photophysical change in the nanocrystal emission, and is not a result of self-absorption losses.

### 4.4.3 Calibrating the Fluorometer

Uncertainty in the LSC OQE measurement is apparent; the uncertainty is due to the number of photons delivered to an LSC and the detector's response to that specific wavelength of light being emitted from the LSC. Varying the light intensity to the detector and measuring the power intensity emitted by the light source via silicon photodiode can calibrate the detector's response.

The first step in calibrating the fluorometer requires placing the excitation fiber optic bundle directly in front of the integration sphere, such that the tip of the fiber optic bundle penetrates the opening of the aperture. The emission slit width was held constant at 14.7 nm, while the excitation slit width was varied. Varying the excitation slit width while holding the emission slit width constant creates a positive linear response in peak integrated area. The second step in calibrating the fluorometer requires placing the excitation fiber optic bundle directly above a silicon photodiode (THORLABS PM100USB). The excitation slit width was varied and the power intensity was monitored. Varying the excitation slit width creates a positive linear response in the power intensity.

The number of photons can be determined using the peak power intensity with equation 4.4,

$$E_{per\ photon} = \frac{hc}{\lambda} \qquad \text{(Equation 4.4)}$$

where h is Plancks constant, c is the speed of light, and λ is the wavelength of light used. Plotting the number of photons per peak area can now create a calibration curve (figure 4.5).

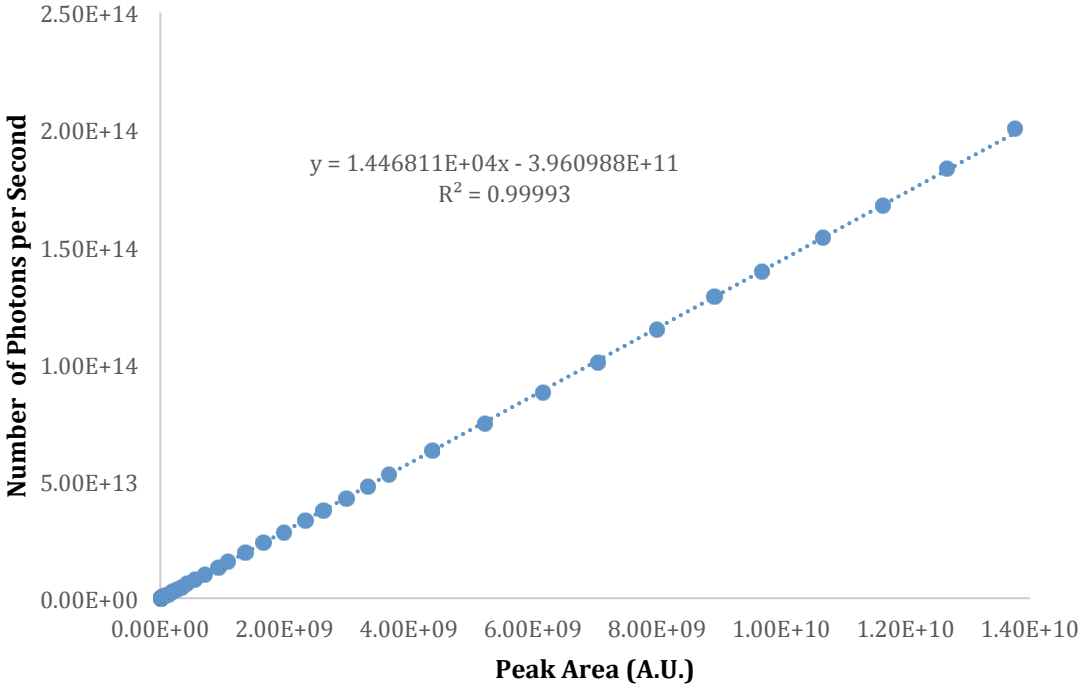


Figure 4.5 Example calibration curve for CIS LSC TK106-1

This linear fit can be used to determine the number of photons per second emerging from the edge of an LSC. The aperture OQE ($OQE_{ap}$) measured over the small edge aperture against the integration sphere can be determined by dividing the number of photons per second out the LSC edge by the number of photons absorbed by the LSC.

### 4.4.4 Experimental Limitations

The integrated photon intensity does not accurately represent the full intensity of photons reaching all edges of a device. This is because the integration

sphere only collects light through a small aperture at one side of the concentrator. Light that is emitted out the other sides of the LSC is not collected; with this in mind the integrated photon intensity would be higher if light was captured around all edges of the LSC.

An air interface exists between the integration sphere and the LSC, and consequently some light that propagates towards the outer side edge of the LSC may not escape out the edge, but instead be reflected back through the waveguide. The same principal that governs TIR and defines an escape cone for light propagation through a waveguide also describes the reflection and refraction at the edge interfaces of the concentrator. Consequently, for a photon to be emitted it must be in an angle within the escape cone. This problematic situation must be accounted for in order to calculate the actual photon intensity out the side edges of an LSC.

For these reasons correction factors must be applied in order to accurately determine actual photon flux out the edges of the LSC. However, correcting for these measurement limitations is not trivial. The correction needs to account for omnidirectional light emission, waveguide attenuation, escape cone, reabsorption, and losses due to luminophore QY.

### 4.4.5 Correction Factor Using the McDowall Model

$OQE_{ap}$ decreases with distance (d) due to both geometric effect (the collection angle subtended by the edge aperture decreases as $tan^{-1}\left(\frac{1}{d}\right)$) and as a result of compounding escape-cone, non-radiative relaxation, and waveguide attenuation losses. The latter is expressed as an optical path length-dependent loss

such that $P = P_0 e^{-\alpha\xi/4.34}$, where $P/P_0$ is the fraction of power remaining after a propagation distance $\xi$ and $\alpha$ (dB cm$^{-1}$) is an attenuation coefficient. The attenuation coefficient accounts for absorbance and scattering by the polymer, nanocrystals, polymer/glass, and glass/air interfaces. The attenuation coefficient ($\alpha$) is treated as wavelength-independent over the narrow emission band of the phosphor. To individually determine attenuation and other losses the McDowall model is used by fiting $OQE_{ap}$ (d) to determine the best $\{\alpha, \Phi\}$ (equation 4.5). Once these parameters are known it becomes possible to compute for any geometric gain the impact of each loss mechanism, as well as the OPE, and edge output irradiance. The model was developed in collaboration with Professor Stephen McDowall from Western Washington University Mathematics department, and is briefly summarized in the following paragraphs.

For a photon absorbed at a location (x, y) to reach the integration sphere, it must be emitted into a wave-guided mode whose path of propagation meets the aperture. During the propagation the photon might be re-absorbed, with a probability determined by the photon's wavelength and the nanocrystals absorption spectrum, and it may be attenuated with a probability determined by α. For this situation all photons that are reabsorbed are treated as lost, even if they have the potential to be re-emitted in a direction to reach the edge aperture.

Setting D to be an illumination window within which solar absorption occurs and denoting $|D|$ to be the area of this window. Let $\Theta(x, y)$ be part of the unit sphere corresponding to guided modes intersecting the aperture. Let $l(x, y, \theta, \phi)$ be

the path length of propagation within the full LSC from (x, y) to the measurement aperture in the direction $(\theta, \phi)$, given in spherical coordinates. Only the central layer of the LSC contains nanocrystals and is considered to be the only layer in which attenuation happens. Let $\xi(x, y, \theta, \phi)$ be the distance of the LSC in which attenuation happens. If Abs (λ) and Em (λ) denote the absorption and emission spectra of the nanocrystals, then:

$$OQE_{ap} = \frac{\Phi}{|D|} \iint_D \frac{1}{4\pi} \iint_{\Theta(x,y)} e^{-\alpha l(x,y,\theta,\phi)} \int Em(\lambda) e^{-Abs(\lambda)\xi(x,y,\theta,\phi)} d\lambda sin\theta d\theta d\phi dA(x,y) \quad \text{(Equation 4.5)}$$

Having estimated the QY and $\alpha$, allows for the determination of the OQE for LSCs with other dimensions. From this it is possible to determine the optical power efficiency and the edge output irradiance. However, for these computations it's no longer appropriate to use the model above since reabsorbed photons have a non-negligible probability of reaching an edge, possibly even after more than one reabsorption/re-emission event. It is assumed that the first reabsorbed photons are uniformly distributed over the LSC, an assumption that comes from ballistic Monte Carlo simulations. Refer to the supplemental information for a complete derivation of the proportion of emitted photons that are lost to attenuation before reaching an edge or being reabsorbed ($S$), and the proportion that are reabsorbed exactly once before reaching an edge or being lost to attenuation ($A$). If $E$ is the proportion lost out the escape cone, then $C = 1 - A - S - E$ is the proportion of initially emitted photons which reach an edge without being absorbed nor attenuated. The AM 1.5 spectral irradiance is integrated against the LSC absorbance to obtain the proportion of incident solar irradiance absorbed by the LSC, and the edge output

irradiance. From this the total proportion of all initially absorbed photons lost to escape cones is $E\Phi(1-A\Phi)^{-1}$; lost to attenuation, $A\Phi(1-A\Phi)^{-1}$; lost due to less than unity QY, $(1-\Phi)(1-A\Phi)^{-1}$; and reaching an edge, $C\Phi(1-A\Phi)^{-1}$.

## 4.5 Physical Characterization of the LSC Polymer

After the spectroscopic characterizations of the LSCs were complete (section 4.4) several samples were disassembled to characterize the LSC polymer/nanocrystal composite. The composites were analyzed by both Fourier-transform infrared spectroscopy (FTIR) and thermogravimetric analysis (TGA).

### 4.5.1 FTIR Characterization

FTIR spectroscopy was used to quantitatively determine the composition of the composite as well as to determine the degree of polymerization. The absorbance of the composite can be thought as being proportional to the number of functional groups responsible for the absorbance process.[60, 61]

In the characterization of the LSC composite a calibration curve was constructed in order to determine the degree of polymerization within the polymer/nanocrystal composite. The calibration curve was constructed by varying the degree of monomer to polymer by weight % in a mixture of 5 standards. The first standard was 100% monomer and changed by 25% by weight monomer/polymer blend until 100% polymer (MW 250,000) was achieved. The calibration curve looked at the absorbance of the alkene peak (1640 $cm^{-1}$) in relative

to the methyl rock peak (1377 $cm^{-1}$). The alkene peak is directly proportional to the degree of polymerization. The disappearance of the alkene peak in the FTIR spectrum can be correlated to a higher degree of polymerization (figure 4.6)

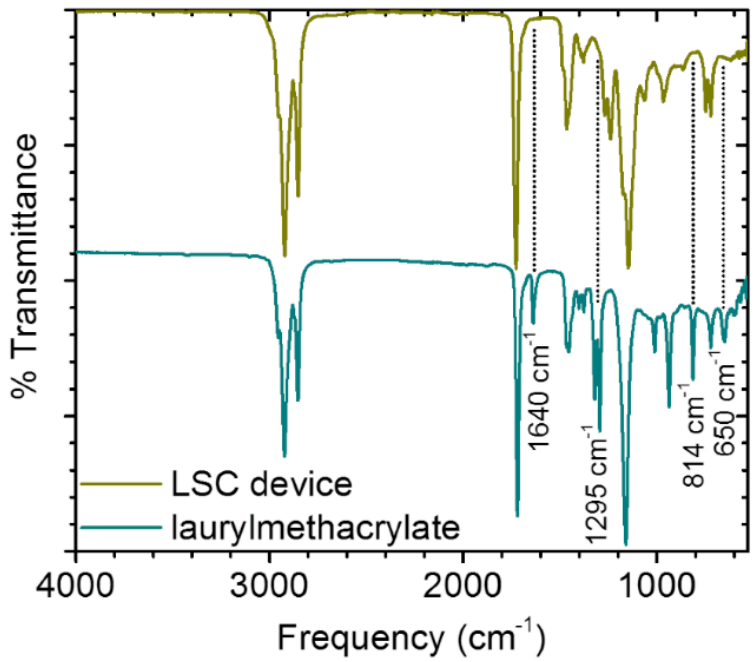


Figure 4.6 FTIR spectra comparing the polymerized composite to laurylmethacryle monomer.

From figure 4.6 it can be seen that the alkene peaks at 1640, 1295, 814, and 650 $cm^{-1}$ are no longer present in the LSC device, indicating undetectable levels of residual monomer. It can be inferred that the LSCs presented in this work are fully polymerized.

### 4.5.2 TGA Characterization

TGA was used to quantitatively measure the weight percent of CIS QDs to polymer. Several samples with varying ODs at 575 nm were measured to determine

the amount of CIS QDs embedded in the polymer. The TGA was ran in the temperature range 25 – 1000 $^{o}$C using TA instruments thermogravimeter. The composite samples were heated at a rate of 20 $^{o}$C min$^{-1}$ under $N_2$ gas with a flow rate of 60 mL min$^{-1}$. The samples were run under nitrogen until 500 $^{o}$C was reached and the carrier gas was switched to compressed air. Degradation began at ~375 $^{o}$C and was complete around 450 $^{o}$C as shown in figure 4.7. The remaining mass in the spectrum at 540 $^{o}$C arises from the NCs.

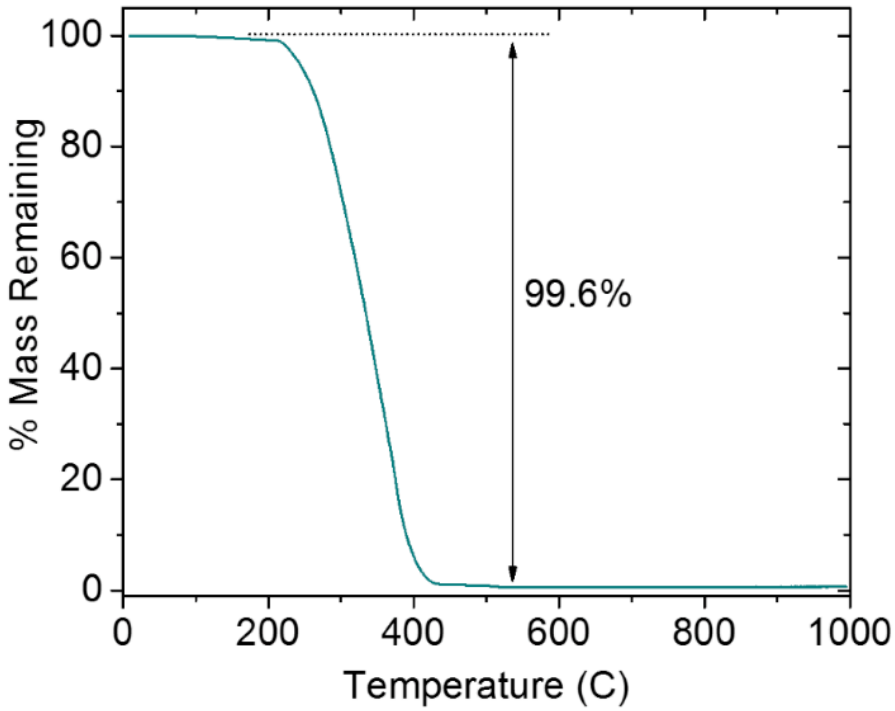


Figure 4.7 Thermogravimetric analysis of composite to determine NC weight percent.

# Chapter 5: Results and Discussion

Using the model developed by our collaborator Prof Stephen McDowall (section 4.4.5) the apparent OQE data (figure 5.1) can be used to compute the full OQE for the LSC. Given the knowledge of the full OQE, it is possible to make meaningful predictions about the performance of LSCs as they are scaled up to larger, more appropriate commercial applications.

## 5.1 Revisiting LSC Measurements

The absorbance and edge emission of a representative LSC from this work is presented in figure 5.1. Three replicate measurements were performed on orthogonal edges of the LSC and the results were averaged. The energy band gap for this particular LSC is centered ~2.1 eV, with a tail that weakly overlaps the emission centered ~1.6 eV. The overlap results in a gradual loss of guided photons to edge of the LSC. This effect is apparent from figure 5.1 where the higher energy photons are lost with increasing optical path length. The decrease in intensity is attributed to geometric effects and waveguide attenuation (section 4.4.5).

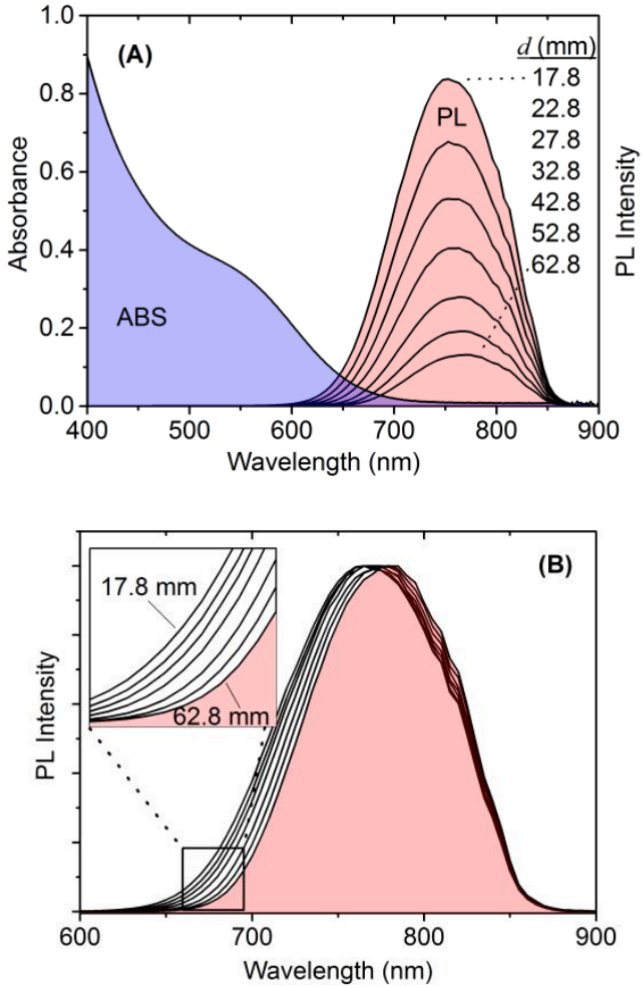


Figure 5.1 Absorption and emission spectrum of CIS LSC device presented in this work. (A) Absorption and emission spectrum as a function of distance d between the excitation spot and LSC edge. (B) Normailized emission intensity showing the loss of higher energy photons w/ increased optical path length.

In devices prepared with high QD concentration, it becomes evident that scattering begins contributing to the total extinction. This effect is illustrated in figure 5.2.

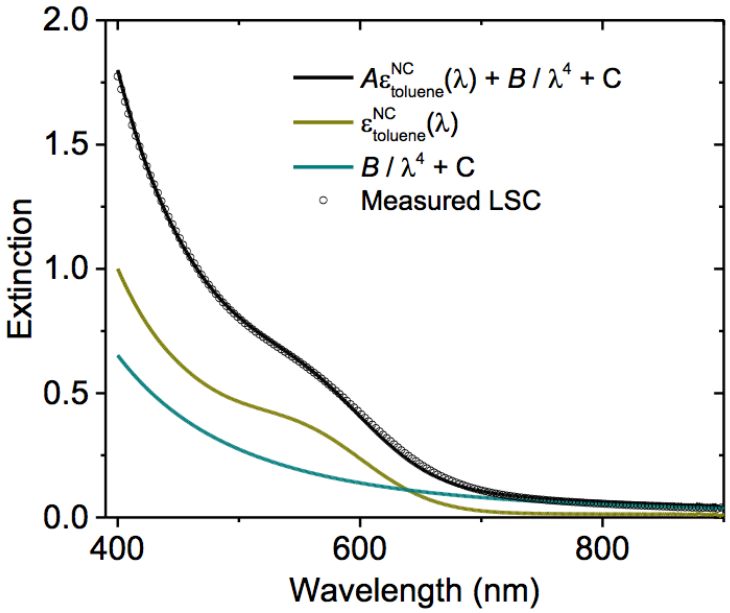


Figure 5.2 Determination of nanocrystal absorbance to total extinction in LSC devices.

The LSC shown in figure 5.2 contains 2.6 wt% CIS: PLMA, having a total extinction coefficient of 0.36 $mm^{-1}$ at a wavelength of 575 nm, corresponding to the first excitation maximum. To individually separate the components such as nanocrystal absorption and scattering we can make use of the fact that the absorption spectra of the nanocrystals were virtually unchanged going from toluene to PLMA. Using this fact a function was created (equation 5.1) to fit to the measured spectra

$$\epsilon_{total}(\lambda) = A\epsilon^{NC}_{toluene}(\lambda) + \frac{B}{\lambda^4} + C \qquad \text{(Equation 5.1)}$$

where $\epsilon^{NC}_{toluene}$ is the normalized absorbance spectrum measured in toluene, and A, B, and C are fitting constants. The first term (A) accounts for NC absorption, the second (B) for scattering, and the third (C) for Fresnel reflections that occur at the glass/air and glass/polymer interfaces.

Integrating the areas under the corrected absorption and emission (figure 5.3 & 5.4) gives the fraction of photons absorbed by the LSC that reach the collection aperture of the integration sphere. Calculating the $OQE_{ap}$ from the aforementioned integrated areas, we are then able to use the McDowall model (figure 5.3).

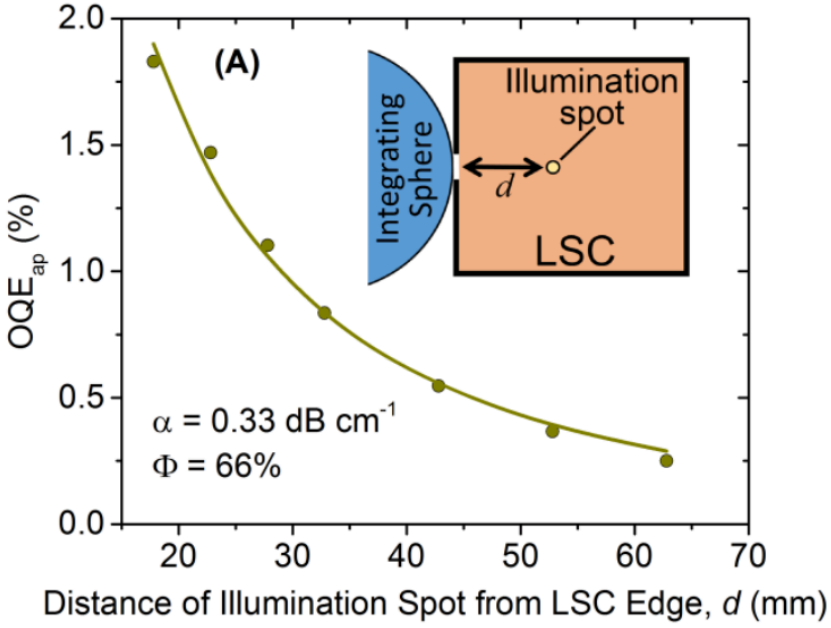


Figure 5.3 LSC characterization and projected performance.

The data points in figure 5.3 represent the $OQE_{ap}$ and the line is the fit from the McDowall model, which is in a good agreement with the experimental data. Using this model allows for predictions about LSC performance as they increase in size.

## 5.2 Geometric Gain

As the LSC increases in size we wanted to see how the performance would vary with geometric gain (equation 2.1).

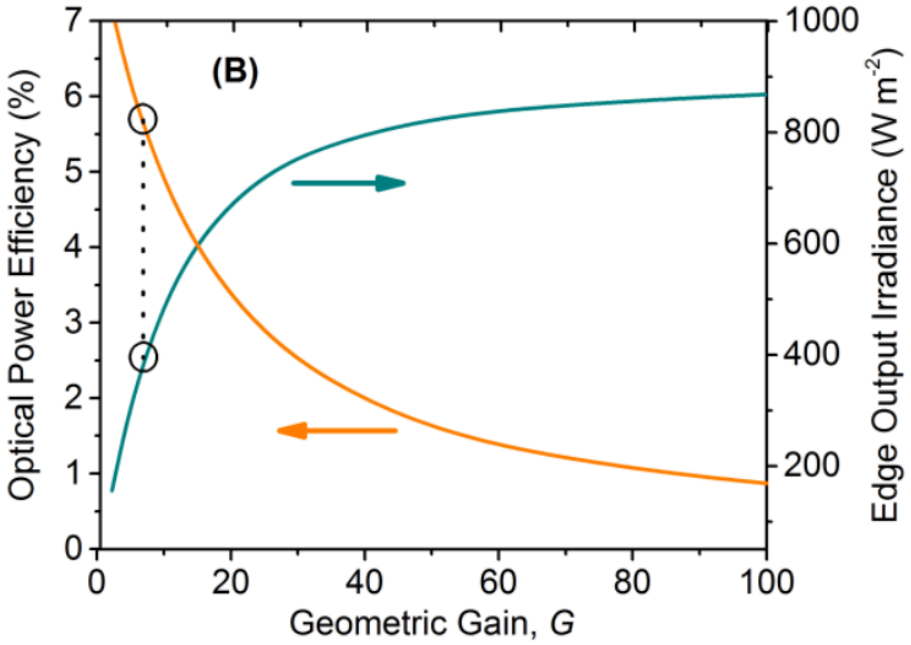


Figure 5.4. Dependence of OPE and edge output irradiance on geometric gain.

From figure 5.6 we can see that the OPE decreases with an increasing geometric gain as waveguide attenuation losses grow with concentrator size; simultaneously the collection area is increasing in size thus increasing the solar irradiance absorption rate. The circle points correspond to the LSC stated from section 5.1. The edge output irradiance approaches a limiting value of ~900 W $m^{-2}$ at a geometric gain ≥ 100, which would correspond to a square LSC with an edge length ≥ 2.8 m. Under full area illumination the experimental LSC with dimension of 75 x 75 mm achieved an OPE = 5.6% at a geometric gain equal to 6.7x and at a geometric gain of 10x the projected OQE was found to be 4.7%. This LSC represents a near 50% improvement over the next best performing activated NC, phosphor, $CuInSe_2$, for a device of the same geometric gain.[29]

Next we wanted to see how parasitic attenuation, non-radiative relaxation, and escape-cone losses depend on geometric gain.

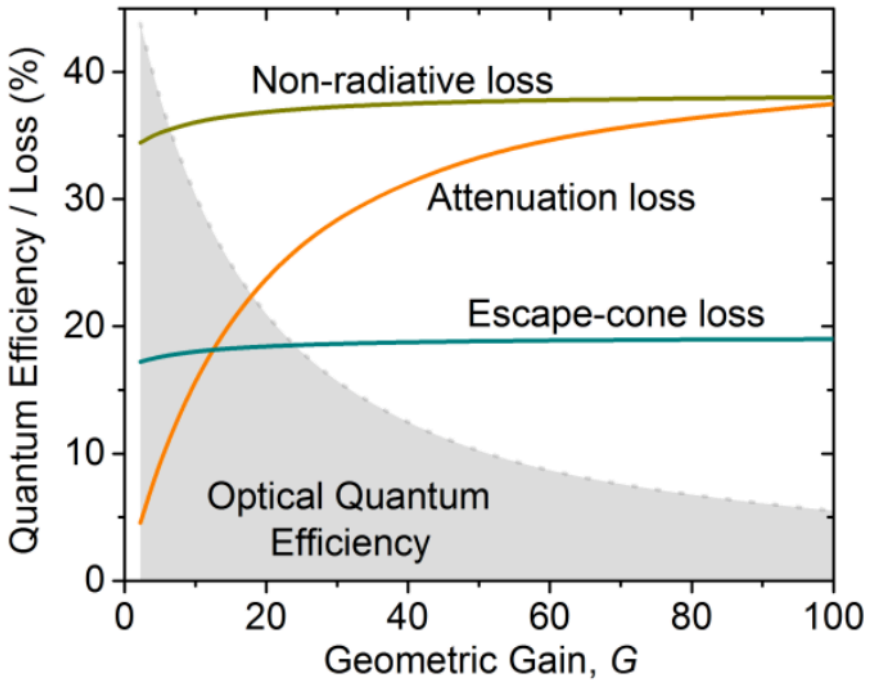


Figure 5.6. Optical loss mechanisms.

From figure 5.6 we see that for an LSC with a geometric gain ≤ 100x, nonradiative relaxation presents the largest loss, followed by escape cone losses. This factor is consistent with the measured QY, which gives a 34% chance for the photon to be lost non-radiatively every time an absorption occurs. As the LSC increases in geometric gain one would expect the escape cone and non-radiative losses to continue to increase with geometric gain due to greater portions of multiple re-absorption/ re-emission events. However, over large propagation distances attenuation rapidly increases and it becomes more likely that a photon will be lost

to attenuation then be absorbed, which would be lost to an escape cone or non-radiatively.

### 5.3 Nanocrystal Loading and Attenuation

Section 5.2 showed how parasitic attenuation dominates efficiency in larger LSCs. To further investigate this concept a series of LSCs were prepared having different nanocrystal loading weights (Figure 5.7).

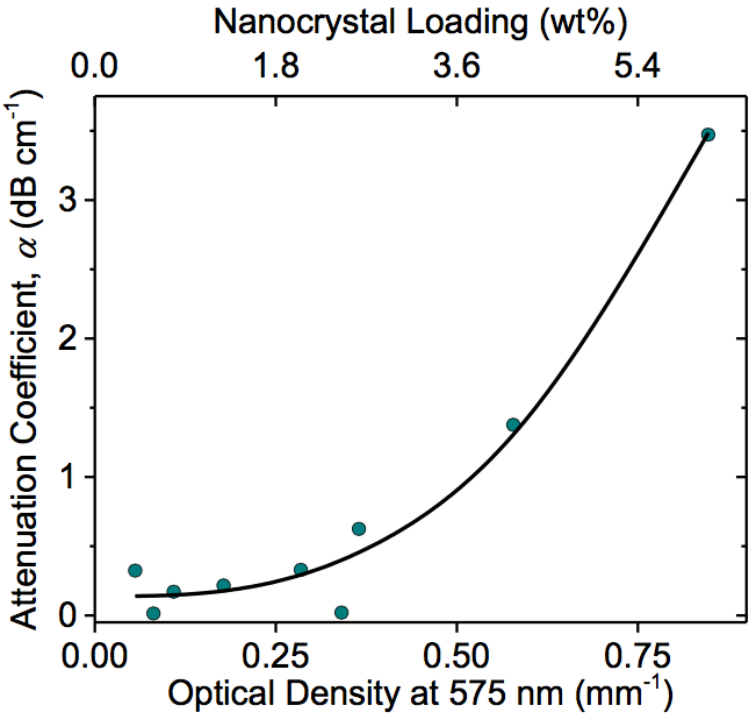


Figure 5.7 Dependence of waveguide attenuation on nanocrystal loading.

The data from figure 5.8 was fit using an attenuation function

$$\alpha = \alpha_0 + \beta c_0 + \gamma c_0^3 (1 + \delta C_0^{2/D})^{-D/2} \qquad \text{(Equation 5.2)}$$

where $c_0$ represents the nanocrystal concentration, D is the fractal dimensions of the nanocrystal clusters postulated to form at sufficiently high concentration by

aggregation, and $\alpha_0, \beta, \gamma, and\ \delta$ are constants. The first term of equation 5.2 accounts for intrinsic propagation losses in the absence of the nanocrystals. The attenuation would arise from absorption and scattering by the polymer, impurities, and from imperfections of the LSC. The second and third terms describe scattering from single nanocrystals and aggregates.[62] For a fractal dimension, D=1.8, an intrinsic attenuation rate $\alpha_0 = 0.14$ dB cm$^{-1}$ was found with negligible single scattering losses corresponding to $\beta = 0$. The data are consistent with an estimate of the Rayleigh scattering cross-section, indicating that the individual nanocrystals are 1-2 orders of magnitude too small to account for the observed attenuation. This observation was also consistent with the Gamelin research group from UW who found no significant scattering for similar CIS QDs in toluene for an optical pathlength approaching 1 m.[57]

At lower nanocrystal loadings α was found to be dominated by intrinsic waveguide losses. The intrinsic attenuation can be attributed to optical-grade methacrylate polymers (~1 x 10$^{-3}$ dB cm$^{-1}$) and glass cladding (1.8 x 10$^{-4}$ dB cm$^{-1}$), suggesting $\alpha_0$ could be made smaller through purification/fabrication methods.[63, 64] However, at concentrations $c_0 \geq \sim 2$ wt% scattering from nanocrystal aggregates starts to dominate, as evident from the cubic attenuation scaling factor of equation 5.2. This result can be understood by the fact that aggregation reduces the number density of scattering objects by a factor of n$^{-1}$, where n is the number of nanocrystals per aggregate; the scattering cross section of the aggregates though increases by a

rate of $n^{2}$.[63] This factor shows the high importance of luminophore dispersion in nanocrystal LSCs, which is critical to creating an effective LSC.

Scattering losses and absorbed solar irradiance both scale in an LSC as the nanocrystal concentration increases, so there must exist a geometric gain with an optimal concentration for maximizing OPE illustrated in figure 5.8.

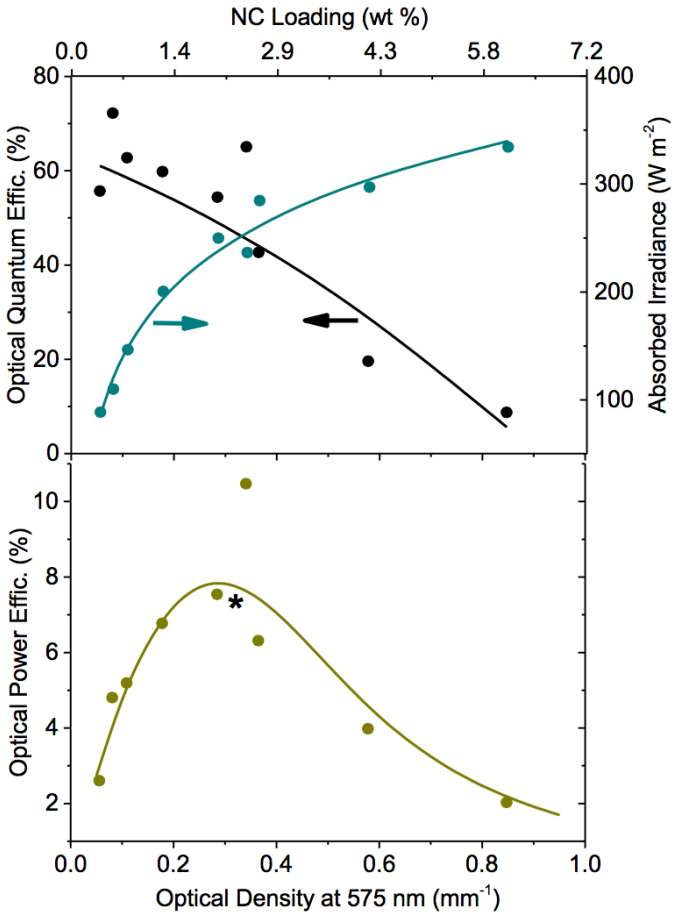


Figure 5.8 LSC performance normalized to a QY of 1.

From figure 5.8 we can see that as the absorbed solar irradiance and optical density increases the OQE decreases. Consequently, the OPE approaches a local geometric gain dependent maximum with an optical density equal to ~0.3 mm. The asterisk

star in the figure represents the LSC from section 5.1. The other solid points are LSCs presented in this work.

Further, we apply these results to examine the performance for CIS nanocrystal LSCs if further improvements identified can be made to α and the QY. As previously stated, the QY can decrease as much as 30% upon incorporation of the nanocrystals into the polymer matrix. The observed parasitic attenuation loss rate is 10-100 times greater than the intrinsic materials themselves. Since these factors limit the overall LSC performance in both small and large devices, significant improvements should be possible to correct these effects. In addition, the host nanocrystal cores could be increased in size thus reducing the energy bandgap, enabling better improvement for solar spectrum matching.

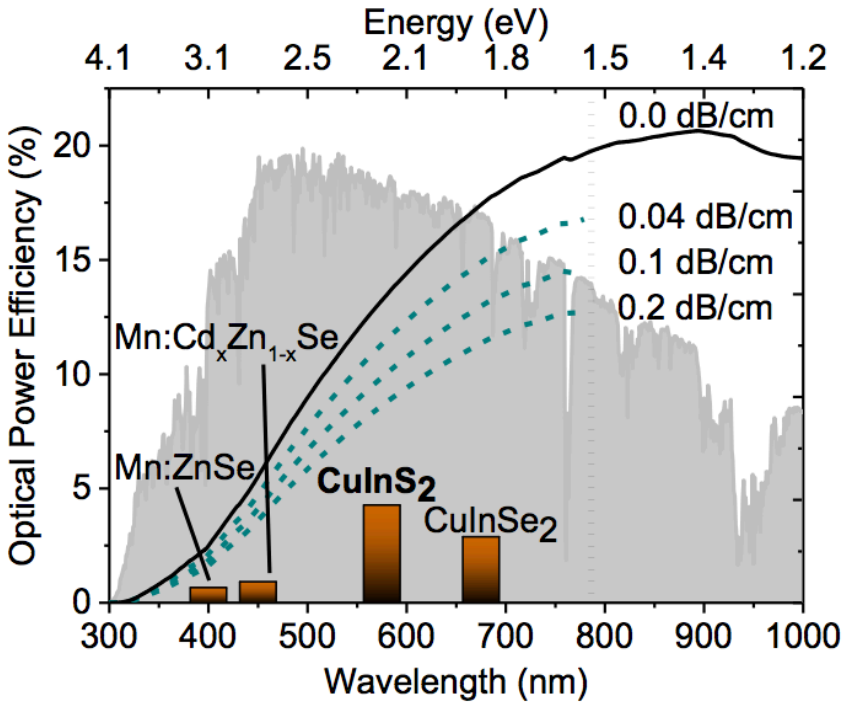


Figure 5.9 Theoretical and actual performance of nanocrystal LSCs.

From Figure 5.9 we see how the performance can be impacted from improvements in the areas stated for devices with G = 10x. The dashed lines assume a QY = 86%,[57] the current highest reported QY for CIS nanocrystals, along with complete solar absorbance up to the indicated band gap. The dashed lines projects OPE for given rates of attenuation (α). The solid line represents an ideal situation where the QY = 100% , α = 0 , 500 meV Stokes shift, zero self-absorption, and one escape-cone loss. These calculations predict efficiencies in the range of 10-15% should be achievable for CIS LSCs. In addition are shown the experimental results from QD LSCs prepared using Mn:ZnSe/ZnS,[23] Mn:$Cd_xZn_{1-x}Se$/CdS,[65] $CuInSe_2$/ZnSe,[29] and CIS from this work. The CIS LSC achieves the highest performance reported for this class of concentrator, and among the best performance for any reported LSC at a comparable geometric gain.

## 5.4 Conclusion

In conclusion, this thesis reports high performing LSCs with an OPE of 5.6% under AM1.5 illumination and >350 W $m^{-2}$ of edge output irradiance centered at 1.6 eV for a geometric gain of 6.7x. A new analytical model developed by professor Stephen McDowall was introduced that enables quantitative analysis for each principle loss mechanism on the basis of straightforward luminophore concentration and excitation dependent measurements without the need for ray-tracing or Monte Carlo simulations. Application of this model allowed for the determination of how concentration affects waveguide efficiency, leading to an optimal concentration corresponding to an optical density of about 0.3 $mm^{-1}$ at the

first absorbance maximum, equivalent to ~2 wt% of nanocrystal content. An analysis of optical losses using a newly introduced analytical model shows that non-radiative relaxation losses dominates at small geometric gain, with scattering losses from nanocrystal aggregates become the limiting factor for larger devices. With further improvements, the projected limiting efficiency in high gain devices is 10%-15%, making CIS QDs well suited for large area, high performance LSCs.

## References


1. International Energy Outlook 2013. August 31, 2013 ed.; U.S. Energy Information Administration: Washington, DC, 2013; p 4.

2. Global Fossil-Fuel CO2 Emissions. http://cdiac.ornl.gov/trends/emis/tre_glob.html (accessed October 6, 2015).

3. Trends In Atmospheric Carbon Dioxide http://www.esrl.noaa.gov/gmd/ccgg/trends/ (accessed October 6, 2015).

4. Peter M. Cox, R. A. B., Chris D. Jones, Steven A. Spall, Ian J. Totterdell, Acceleration of Global Warming Due to Carbon-Cycle Feedbacks in a Coupled Climate Model. *Nature* **2000,** *408*, 184-187.

5. Mark Jacobson, M. D., Providing All Global Energy With Wind, Water, and Solar Power, Part I: Technologies, Energy Resources, Quantities and Areas of Infrastructure, and Materials. *Energy Policy* **2011,** *39*, 1154-1169.

6. Hydroelectric Power Water Use. http://water.usgs.gov/edu/wuhy.html.

7. Graf, W., Downstream Hydrologic and Geomorphic Effects of Large Dams on American River. *Geomorphology* **2006,** *79* (3-4), 336-360.

8. Fangrui Ma, M. H., Biodiesel Production: A Review. *Bioresource Technology* **1999,** *70* (1), 1-15.

9. Timothy Searchinger, R. H., R. Houghton, Fengxia Dong, Amani Elobeid, Jacinto Fabiosa, Simla Tokgoz, Dermot Hayes, Tun-Hsiang Yu, Use of U.S. Croplands for Biofuels Increases Greenhouse Gases Through Emission from Land-Use Change. *Science* **2008,** *319* (5867), 1238-1240.

10. Solar Power. http://environment.nationalgeographic.com/environment/global-warming/solar-power-profile/ (accessed October 19, 2015).

11. Cyrus Wadia, A. A., Daniel Kammen, Materials Availability Expands the Opportunity for Large-Scale Photovoltaics Deployment. *Environmental Science Technology* **2009,** *43*, 2072-2077.

12. Ramesh, R., SunShot Vision Study. Energy, D. o., Ed. National Renewable Energy Laboratory: 2012; pp 1-292.

13. G. Giroult-Matlakowski, U. T., A. Blakers, Photovoltaic Market Analysis. In *15th EC PVSEC*, Centre for Sustainable Energy Systems: Vienna, 1998.

14. Pablo Benitez, J. C. M., Pablo Zamora, Ruben Mohedano, Aleksandra Cvetkovic, Marina Buljan, Julio Chaves, Maikel Hernandez, High Performance Fresnel-Based Photovoltaic Concentrator. *Optics Express* **2010,** *18* (S1), A25-A40.

15. Concentrating Solar Power: Technologies, Cost, and Performance. http://www1.eere.energy.gov/solar/pdfs/svs_chapter_5_csp.pdf (accessed October 7, 2015).

16. Concentrating Solar Power Dish/Engine System Basics. http://energy.gov/eere/energybasics/articles/concentrating-solar-power-dishengine-system-basics (accessed October 22, 2015).

17. Rob W. Andrews, A. P., Joshua M. Pearce, Photovoltaic System Performance Enhancement with Non-Tracking Planar Concentrators: Experimental Results and BDRF Based Modelling. In *2013 IEEE 39th Photovoltaic Specialists Conference (PVSC)*, 2013.

18. Suljo Linic, P. C., David Ingram, Plasmonic-Metal Nanostructures for Efficient Conversion of Solar to Chemical Energy. *Nature* **2011,** *10*, 911-921.

19. Harry Atwater, A. P., Plasmonics for Improved Photovoltaic Devices. *Nature* **2010,** *9*, 205-213.

20. B. Swartz, T. C., A. Zewail, Photon Trapping and Energy Transfer in Multiple-Dye Plastic Matrices: An Efficient Solar-Energy Concentrator. *Optics Letters* **1977,** *1* (2), 73-75.

21. A. Goetzberger, W. G., Solar Energy Conversion with Fluorescent Collectors *Applied Physics* **1977,** *14*, 123-139.

22. J. Levitt, W. W., Materials for Luminescent Greenhouse Solar Collectors. *Applied Optics* **1977,** *16* (10), 2684-2689.

23. Christian Erickson, L. B., Stephen McDowall, John Gilbertson, Daniel Gamelin, David Patrick, Zero-Reabsorption Doped-Nanocrystals Luminescent Solar Concentrators. *ACS NANO* **2014,** *8* (4), 3461-3467.

24. W. Weber, J. L., Luminescent Greenhouse Collector for Solar Radiation. *Applied Optics* **1976,** *15* (10), 2299-2300.

25. Ralf B. Wehrspohn, U. R., Andreas Gombert, *Photon Management in Solar Cells*. 1st ed.; Wiley-VCH: 2015.

26. Uwe Rau, F. E., Gerda Glaeser, Efficiency Limits of Photovoltaic Fluorescent Collectors. *Applied Physics Letters* **2005,** *87*, 171101-1 - 171101-3.

27. Sark, W. G. J. H. M. V., Recent Developments in Luminescent Solar Concentrators. In *Next Generation Technologies for Solar Energy Conversion V*, Oleg Sulima, G. C., Ed. SPIE: 2014; Vol. 9178, pp 917804-1 - 917804-9.

28. J. Sansregret, J. D., W. Thomas, and M. Lesiecki, Light Transport in Planar Luminescent Solar Concentrators: The Role of DCM Self-Absorption. *Applied Optics* **1983,** *22* (4), 573-577.

29. Francesco Meinardi, H. M., Francesco Carulli, Annalisa Colombo, Kirill A. Velizhanin, Nikolay S. Makarov, Roberto Simonutti, Victor I. Klimov, Sergio Brovelli, Highly Efficient Large-Area Colourless Luminescent Solar Concentraors Using Heavy-Metal-Free Colloidal Quantum Dots. *Nature* **2015,** *10*, 878-885.

30. A. J. Chatten, D. F., C. Jermyn, P. Thomas, B. F. Buxton, A. Buchtemann, R. Danz, K. W. J. Barnham Thermodynamic Modelling of Luminescent Solar Concentrators. In *Proceedings of the Photovoltaic Specialists Conference*, London, 2005.

31. Kurtz, S., Opportunities and Challenges for Development of a Mature Concentrating Photovoltaic Power Industry. NREL, Ed. 2008.

32. E. Fred Schubert, T. G., Jong Kyu Kim, *Light Emitting Diodes*. Kirk-Othmer Encyclopedia of Chemical Technology: 2005.

33. Tien, P. K., Light Waves in Thin Films and Integrated Optics. *Applied Optics* **1971,** *10* (11), 2395-2413.

34. Robert Siegel, J. R. H., *Thermal Radiation Heat Transfer*. Hemisphere Publishing Corporation: 1992.

35. Michael Currie, J. M., Timothy Heidel, Shalom Goffri, Marc Baldo, High-Efficiency Organic Solar Concentrators for Photovoltaics. *Science* **2008,** *321* (5886), 226-228.

36. Maud J. Kastelijn, C. W. M. B., Michael G. Debije, Influence of Waveguide Material on Light Emission in Luminescent Solar Concentrators. *Optical Materials* **2009,** *31* (11), 1720-1722.

37. Francesco Meinardi, A. C., Kirill Velizhanin, Roberto Simonutti, Monica Lorenzon, Luca Beverina, Ranjani Viswanatha, Victor Klimov, Sergio Brovelli, Large-area Luminescent Solar Concentrators based on 'Stokes-Shift-Engineered' Nanocrystals in a Mass-Polymerized PMMA Matrix. *Nature* **2014,** *8*, 392-399.

38. Alessandro Sanguineti, M. S., Riccardo Turrisi, Riccardo Ruffo, Gianfranco Vaccaro, Francesco Meinardi and Luca Beverina, High Stokes Shift Perylene Dyes for Luminescent Solar Concentrators. *Chemical Communications* **2013**.

39. Steve McDowall, B. J., David Patrick, Simulations of Luminescent Solar Concentrators: Effects of Polarization and Fluorophore Alignments. *Journal of Applied Physics* **2010,** *108*.

40. Finn Purcell-Milton, Y. G. k., Quantum Dots for Luminescent Solar Concentrators. *Journal of Materials Chemistry* **2012,** *22*, 16687-16697.

41. Peter Reiss, M. P., Liang Li, Core/Shell Semiconductor Nanocrystals. *Small-Journal* **2009,** *5* (2), 154-168.

42. Igor Coropceanu, M. B., Core/Shell Quantum Dot Based Luminescent Solar Concentrators. *Nano Letters* **2014**.

43. Willie E. Benjamin, D. R. V., Matt J. Perkins, Edward Bain, Kelsey Scharnhorst, Stephen McDowall, David L. Patrick, John D. Gilbertson, Sterically Engineered Perylene Dyes for High Efficiency Oriented Fluorophore Luminescent Solar Concentrators. *Chemical Materials* **2014,** *3* (26), 1291-1293.

44. Stephen McDowall, T. B., Edward Bain, Kelsey Scharnhorst, David Patrick, Comprehensive Analysis of Escape-Cone Losses from Luminescent Waveguides. *Applied Optics* **2013,** *52* (6), 1230-1239.

45. Rowan W. MacQueen, Y. Y. C., Raphael G.C.R. Clady, Timothy W. Schmidt, Towards an Aligned Luminophore Solar Concentrator. *Optics Express* **2010,** *18* (S2), A161-A166.

46. C.L. Mulder, P. D. R., A. M. Velazquez, H. Kim, C. Rotschild, M.A. Baldo, Dye Alignment in Luminescent Solar Concentrators: I. Vertical Alignment for Improved Waveguide Coupling. *Optics Express* **2010,** *18* (S1), A79-A90.

47. Paul P. C. Verbunt, S. T., Michael G. Debije, Dirk. J. Boer, Cees W.M. Bastiaansen, Chi-Wen Lin, Dick K. G. de Boer, Increased Efficiency of Luminescent Solar Concentrators After Application of Organic Wavelength Selective Mirrors. *Optics Express* **2012,** *20* (S5), A655-A668.

48. Jan Christoph Goldschmidt, M. P., Liv Pronneke, Lorenz Steidl, Rudolf Zentel, Benedikt Blasi, Andreas Gombert, Stefan Glunz, Gerhard Willeke, and Uwe Rau, Theoretical and Experimental Analysis of Photonic Structures for Fluorescent Concentrators with Increased Efficiencies. *Phys. Stat. Sol.* **2008,** *205* (12), 2811-2821.

49. Schropp, Z. K. W. G. J. G. M. v. S. C. d. M. D. R. E. I. In *Exploration of Parameters Influencing the Self-Absorption Losses in Luminescent Solar Concentrators with an Experimentally Validated Combined Ray-Tracing/Monte-Carlo Model*, High and Low Concentrator Systems for Solar Electric Applications VIII, Plesniak, A. P., Ed. SPIE: 2013.

50. Remi Beaulac, P. I. A., Stefan T. Ochsenbein, Daniel R. Gamelin, Mn2+ - Doped CdSe Quantum Dots: New Inorganic Materials for Spin-Electronics and Spin-Photonics. *Advanced Functional Materials* **2008,** *18* (24), 3873-3891.

51. Liam R. Bradshaw, A. H., Emily J. McLaurin, Daniel R. Gamelin, Luminescence Saturation via Mn 2+ - Exciton Cross Relaxation in Colloidal Doped Semiconductor Nanocrystals. *Journal Physical Chemistry C* **2012,** *116* (16), 9300-9310.

52. William M. Yen, S. S., Hajime Yamamoto, *Phosphor Handbook*. CRC Press: Boca Raton, Florida, 2007.

53. William D. Rice, H. M., Victor I. Klimov, Scott A. Crooker, Magneto-Optical Properties of CuInS2 Nanocrystals. *J. Phys. Chem. Lett.* **2014,** *23* (5), 4105-4109.

54. Kathryn E. Knowles, K. H. H., Troy B. Kilburn, Arianna Marchioro, Heidi D. Nelson, Patrick J. Whitham, Daniel Gamelin, Luminescent Colloidal Semiconductor Nanocrystals Containing Copper: Synthesis, Photophysics, and Applications. *Chemical Reviews* **2016**, A-Y.

55. Liam R. Bradshaw, K. E. K., Stephen McDowall, Daniel R. Gamelin, Nanocrystals for Luminescent Solar Concentrators. *Nano Letters* **2015,** *15*, 1315-1323.

56. Haizheng Zhong, S. S. L., Tihana Mirkovic, Yunchao Li, Yuqin Ding, Yongfang Li, Gregory D. Scholes, Noninjection Gram-Scale Synthesis of Monodisperse Pyramidal CuInS2 Nanocrystals and Their Size-Dependent Properties. *ACS NANO* **2010,** *9* (4), 5253-5262.

57. Kathryn E. Knowles, T. B. K., Dane G. Alzate, Stephen McDowall, Daniel R. Gamelin, Bright CuInS2/CdS Nanocrystal Phosphors for High-Gain Full-Spectrum Luminescent Solar Concentrators. *Chemical Communications* **2015,** *51*, 9129-9132.

58. Lian Li, A. P., Donald J. Werder, Bishnu P. Khanal, Jeffrey M. Pietryga, Victor I. Klimov, Efficient Synthesis of Highly Luminescent Copper Indium Sulfide-Based Core/Shell Nanocrystals with Surprisingly Long-Lived Emission. *Journal of American Chemical Society* **2011,** *133*, 1176-1179.

59. Lakowicz, J. R., *Principles of Fluoresence Spectroscopy*. 3rd ed.; Springer Science & Business Media: 2007.

60. Baxter A, D. M., Taylor KD, Roberts GA, Improved Method for I.R. Determination of the Degree of N-Acetylation of Chitosan. *Int J Biol Mac* **1992,** *3* (14), 166-9.

61. Khan TA, P. K., Ch'ng HS, Reporting Degree of Deacetylation Values of Chitosan: The Influence of Analytical Methods. *J Pharm Pham Sci* **2002,** *3* (5), 205-12.

62. Ryan Sumner, S. E., Troy B. Kilburn, Christian Erickson, Brian Carlson, Daniel R. Gamelin, Stephen McDowall, David L. Patrick, High Efficiency CuInS2/CdS Nanocrystal Luminescent Solar Concentrators. Western Washington University: 2016; pp 1-18.

63. Toshikuni Kaino, M. F., Shigeru Oikawa, Shigeo Nara, Low-loss Plastic Optical Fibers. *The Optical Society* **1981,** *20* (17), 2886-2888.

64. Schott Optical Glass Description of Properties. Manufacture's Literature, 2011.

65. Christian Erickson, L. B., Stephen McDowall, John Gilbertson, Daniel Gamelin, David Patrick, Unpublished Work.